ISPRS Journal of Photogrammetry and Remote Sensing 178 (2021) 1–19

Contents lists available at ScienceDirect

ISPRS Journal of Photogrammetry and Remote Sensing

journal homepage: www.elsevier.com/locate/isprsjprs

A semi-empirical scheme for bathymetric mapping in shallow water by ICESat-2 and Sentinel-2: A case study in the South China Sea

Hsiao-Jou Hsu [a], Chih-Yuan Huang [a,b], Michael Jasinski [c], Yao Li [d], Huilin Gao [d], Tsutomu Yamanokuchi [e], Cheng-Gi Wang [f], Tse-Ming Chang [f], Hsuan Ren [b], Chung-Yen Kuo [g], Kuo-Hsin Tseng [a,b,*]

[a] Department of Civil Engineering, National Central University, Taoyuan 32001, Taiwan
[b] Center for Space and Remote Sensing Research, National Central University, Taoyuan 32001, Taiwan
[c] National Aeronautics and Space Administration, Goddard Space Flight Center, Greenbelt, MD 20771, USA
[d] Zachry Department of Civil and Environmental Engineering, Texas A&M University, College Station, TX 77843, USA
[e] Remote Sensing Technology Center of Japan, Tokyu Reit Toranomon Bldg. 3F, 3-17-1 Toranomon, Minato-ku, Tokyo 105-0001, Japan
[f] Department of Land Administration, Ministry of the Interior, Taipei, Taiwan
[g] Department of Geomatics, National Cheng Kung University, Tainan, Taiwan

ARTICLE INFO

Keywords:
Coastal Bathymetry
Electronic Navigation Chart
Zones of Confidence
LiDAR

ABSTRACT

To derive shallow water bathymetry for coastal areas, a common approach is to deploy a scanning airborne bathymetric light detection and ranging (LiDAR) system or a shipborne echosounder for ground surveys. However, recent advancements in satellite remote sensing, including the Ice, Cloud and land Elevation Satellite-2 (ICESat-2) offer new tools for generating satellite derived bathymetry (SDB). The key payload onboard ICESat-2 is the Advanced Topographic Laser Altimeter System (ATLAS), a micro-pulse, photon-counting LiDAR system, simultaneously emitting six separate 532 nm beams at 10 kHz pulse rate. However, despite its high resolution, the major limitation for bathymetry is that ICESat-2 only provides along-track height profiles, leaving observation gaps between the parallel ground tracks. Merging ICESat-2 observations with optical multispectral imagery, as demonstrated herein, provides an effective solution for deriving a full scene of water depth in light of the spectral attenuation behavior.

This study aims to combine ICESat-2 and Sentinel-2 optical data to derive shallow water bathymetry (depth <20 m) at six islands and reefs in the South China Sea. ICESat-2 ATL03 point clouds of georeferenced photons are first filtered to determine the seafloor elevation along the ground track. Results indicate a root-mean-square error (RMSE) of 0.26–0.61 m as compared with independent observations from an airborne LiDAR campaign. Next, three semi-empirical functions, namely the Modified Linear/Polynomial/Exponential Ratio Models with its kernel formed by the log ratio between Sentinel-2's green and blue bands, are used to fit the spectral data with ICESat-2 height profiles. After water depth mapping using the trained model, independent ICESat-2 point clouds are used to validate the Sentinel-2 derived bathymetry. The RMSE values of the three models using the weighted average of multiple images for these six islands are within 0.50–0.90 m in 0–15 m deep. We also demonstrate that a synthesis of satellite laser altimetry and optical remote sensing can produce SDB results that potentially meet the requirement of category *C* in Zones of Confidence (ZOC) of the Electronic Navigational Chart (ENC) in 0–8 m deep. It is foreseen that ICESat-2 will be a helpful tool for mapping coastal and shallow waters around the world especially where bathymetric data are unavailable.

1. Introduction

Shallow water bathymetry is crucial for coastal construction, navigation safety, resources exploration, and studies about ecosystems along the nearshore and intertidal zones (Dahlgren et al, 2014; McCombs et al, 2014). However, it is a costly and challenging task to use conventional surveying procedures, such as depth profiling by a single/multiple beam echo-sounder or by an airborne light detection and ranging (LiDAR)

* Corresponding author.
E-mail address: khtseng@csrsr.ncu.edu.tw (K.-H. Tseng).

https://doi.org/10.1016/j.isprsjprs.2021.05.012
Received 16 December 2020; Received in revised form 11 May 2021; Accepted 17 May 2021
Available online 3 June 2021

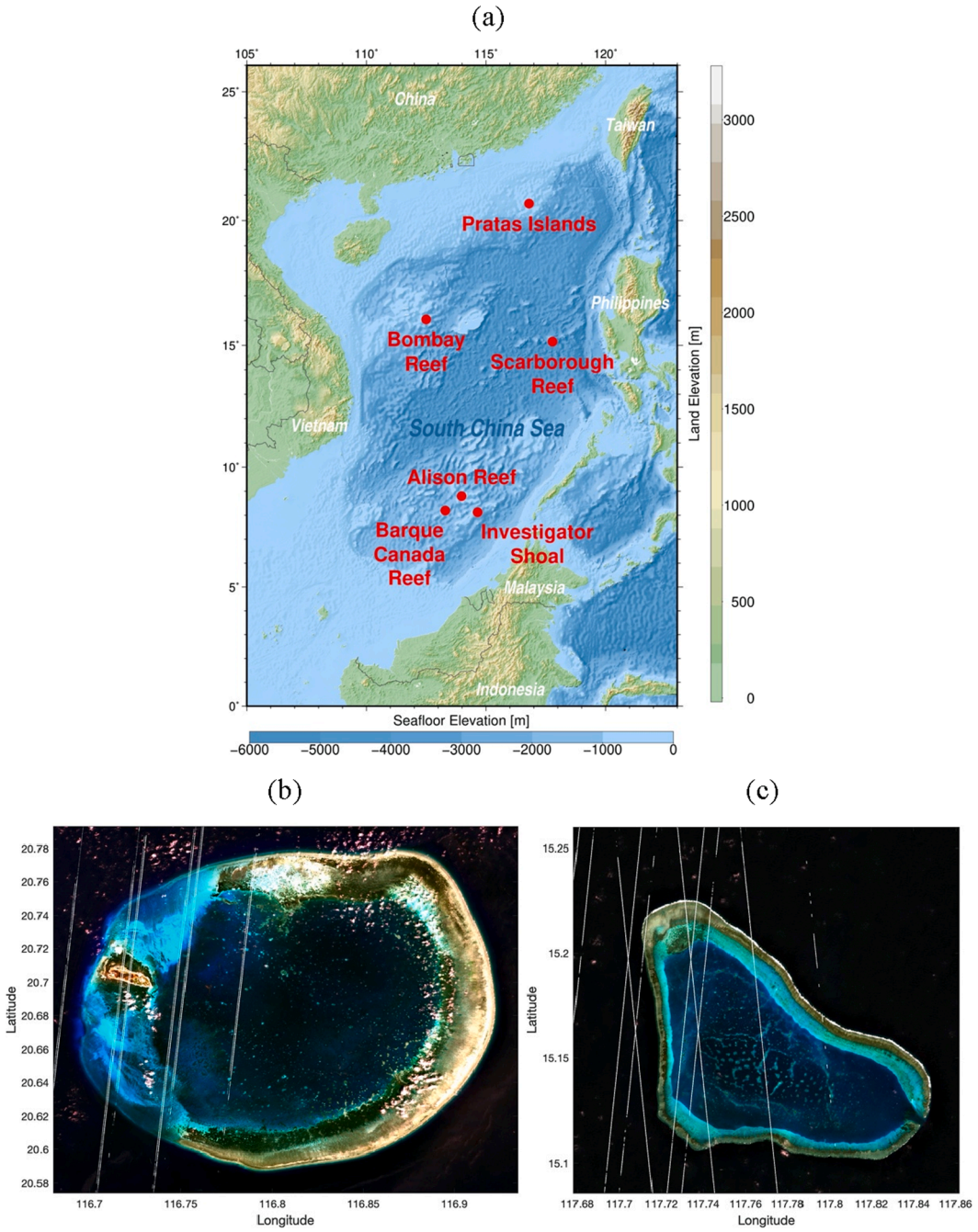

Fig. 1. (a) Main map of the South China Sea and the geolocations of six testing sites. (b–g) Natural color composite of Sentinel-2 images in (b) Dongsha Island, (c) Scarborough Reef, (d) Alison Reef, (e) Bombay Reef, (f) Barque Canada Reef, and (g) Investigator Shoal. White line sectors in each panel (b–g) indicate the ground tracks of ICESat-2 six beams with usable surface reflections in 2018/10–2019/08.

campaign (Pike et al., 2019). Moreover, it is precarious and uneconomical for vessels to navigate into shallow waters (<20 m from sea surface) for profiling the seafloor with a limited field of view. To overcome limitations in mobility and instrumentation, satellite remote sensing technologies have been increasingly utilized for bathymetric mapping. Satellite-derived bathymetry (SDB) is known as a technique to recover water depth on multiple scales by various satellite observables, such as gravity anomalies (Sandwell et al., 2014), photogrammetry (Hodúl et al., 2018), optical imageries (Caballero and Stumpf, 2020), etc. Some commonly seen SDB products by optical imageries include the Landsat series in 30 m (Pacheco et al, 2015; Knudby et al., 2016; Chénier et al., 2018), Sentinel-2 in 10 m (Traganos et al., 2018), or high-resolution Worldview/RapidEye/Pleiades imagers with sub-meter ground sampling distance (GSD) (Chénier et al., 2018; Cahalane et al., 2019). The principle of SDB by optical images takes advantage of the Beer-Lambert law, relating the exponential attenuation of light with the path length it traveled (Lyzenga 1978, 1981). For those shallow waters without direct observations of water depth, the physical-based inversion is needed to solve water quality indicators (e.g., chlorophyll and gelbstoff concentration) and water depth altogether through the optimization of forward modeling (Adler-Golden et al., 2005; Eugenio et al., 2015; Lee et al., 1998, 1999, 2012). However, this approach is preferred for hyperspectral data that provide the detailed inter-band information (Kerr and Purkis, 2018). Also, the calculation of water column thickness

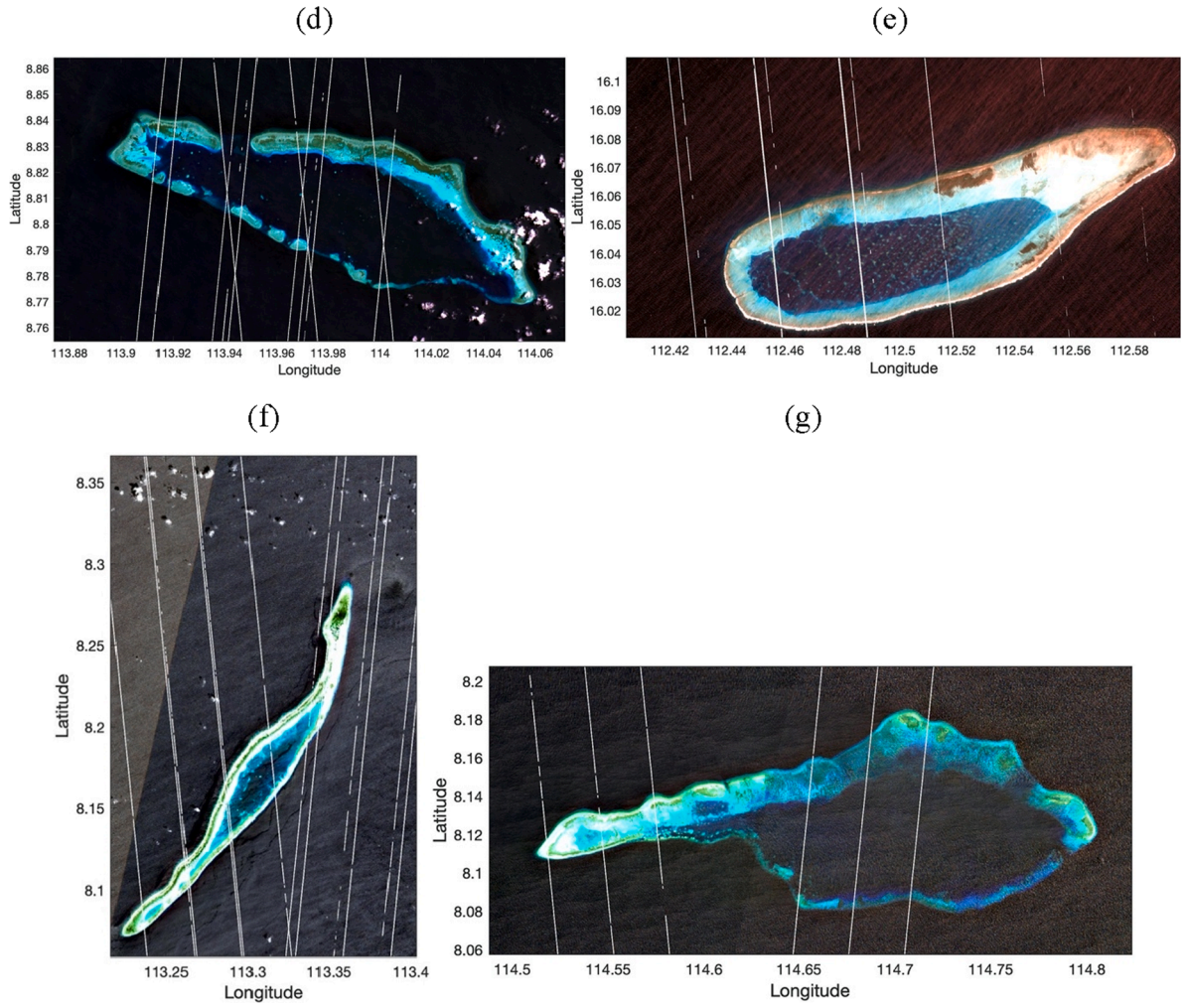

Fig. 1. (*continued*).

is sensitive to several inherent issues for passive remote sensing, e.g., mixed pixels from different substrates types and inconsistent water attenuation coefficients. It is also sensitive, although not strictly limited, to ocean surface conditions (e.g., waves, sun glint, and solar angle). In contrast, for those areas which have scattered in-situ measurements from airborne LiDAR or sonar, the empirical method is used to calibrate the relationship between reflectance and depth (Kerr and Purkis, 2018; Geyman and Maloof, 2019). The major restriction of this approach in many remote islands is the availably and quality of *in-situ* data. Hence, it is worthwhile to examine the possibility of using the Ice, Cloud and land Elevation Satellite-2 (ICESat-2) laser altimetry as necessary training data in the empirical model, especially to fill the gap of missing ground truths in remote islands in the South China Sea (Fig. 1).

ICESat-2 launched in September 2018, features a state-of-the-art spaceborne LiDAR system aiming to measure surface elevations (Markus et al., 2017). As a successor to ICESat that operated from 2003 to 2009, ICESat-2 is equipped with the high resolution Advanced Topographic Laser Altimeter System (ATLAS). ATLAS estimates ranges between the telescope and targets near ground by utilizing a photon counting technique (Neumann et al., 2019b; Martino et al., 2019). The elevations of each photon from a LiDAR pulse that are backscattered to the detector (a tiny fraction of all emitted photons) are georeferenced based on the timing of its round-trip. Although the primary goal of ICESat-2 is to observe elevations of land ice, sea ice, cloud tops, canopy tops, terrain and water surfaces, it has been reported that the subaqueous mapping of shallow water is possible thanks to the water penetration capability of green laser. Forfinski-Sarkozi and Parrish (2016) and Jasinski et al. (2016) demonstrated the potential for employing satellite LiDAR to detect bathymetry in depths of up to 10 m, using the Multiple Altimeter Beam Experimental LiDAR (MABEL), NASA's high altitude airborne ICESat-2 simulator. Li et al. (2019) combined airborne MABEL data and Landsat-based water classifications to derive near-shore bathymetry for Lake Mead. A comparison between MABEL-derived elevation and *in-situ* data showed that the discrepancy, in terms of the root-mean-square error (RMSE), is at 1.18–2.36 m level along four transects. Parrish et al. (2019) evaluated ATLAS's bathymetric mapping performance over St. Thomas of U.S. Virgin Islands. After correcting the refractivity between air–water interface and the reduced speed of light in water, the RMSE, as validated by the Experimental Advanced Airborne Research Lidar-B (EAARL-B) collected by the U.S. Geological Survey (USGS), achieved 0.43–0.60 m for four laser tracks. However, ICESat-2 only provides point measurements along the ground track of six laser beams, which is still insufficient to produce a contour map of seafloor for practical applications, such as the Electronic Navigation Chart (ENC).

The goal of this study is thus to introduce a solution scheme to derive bathymetry in remote islands whose water quality and substrate types may vary and the ground truth data are previously absent. To achieve this goal, an empirical-based approach integrating accurate point measurements of height from ICESat-2 and the multispectral information from Sentinel-2 are used. The novelty of this scheme includes the merge of multiple Sentinel-2 images to reduce random errors resulted from atmospheric or water quality disturbances in any single image. In the following sections, Section 2 introduces the study area and the workflow

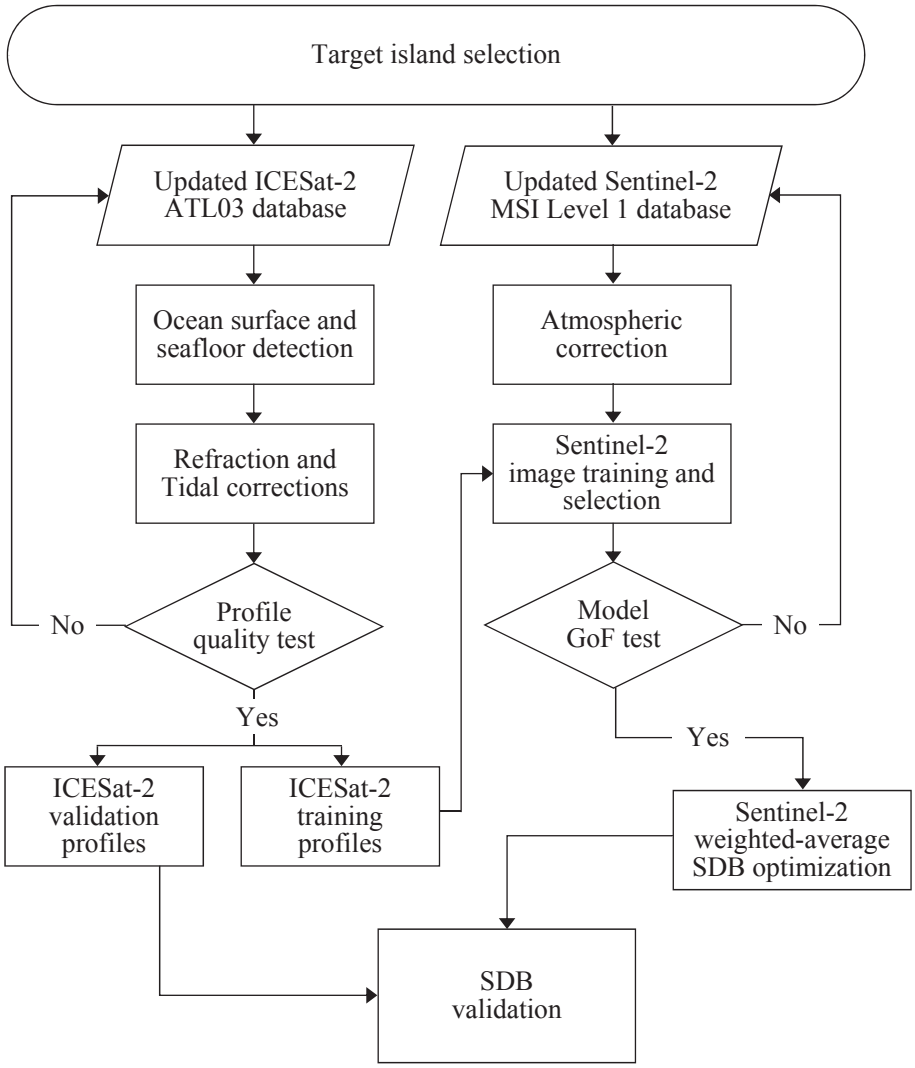

Fig. 2. The framework for generating shallow water bathymetry maps by integrating ICESat-2 ATL03 and Sentinel-2 images.

for filtering the ICESat-2 point cloud. Section 3 describes the processing steps of satellite data and the formation of three models to derive the Sentinel-2 bathymetric map. Section 4 examines sea surface heights measured by ICESat-2 and SDB derived from Sentinel-2. The RMSE of SDB derived from a single image and the prediction of accuracy by the goodness-of-fit (GoF) are demonstrated. The weighted-average SDB is further inspected at different water depths to evaluate the qualification in confidence categories. In Section 5, the error budget and the potential ways to reduce it are discussed. Finally, the conclusions and limitations are summarized in Section 6.

2. Study area and workflow

2.1. Study area

Dongsha Islands (also known as Pratas Island, Fig. 1b) in the northern South China Sea consist of three atolls including Dongsha Atoll and North/South Vereker Atolls. Dongsha Island, located approximately 400 km southwest of Kaohsiung, its administrative city in Taiwan, extends 2.5×0.8 km^2 and is the only coral island above sea level in this region. The atoll is a ring-shaped coral reef with depths ~ 20 m in the lagoon. Dongsha Atoll was named a national park of Taiwan in 2007, owing to its natural landscapes and rich biodiversity. A complete airborne LiDAR campaign had been carried out in September 2010 under the support of the Ministry of the Interior, Taiwan (Shih et al., 2011). Therefore, a bathymetry raster at 5 m resolution interpolated from dense point clouds is available to serve as a validation dataset. As shown in Fig. 1b, a number of submerged reefs exist in the lagoon, making it challenging to map the bathymetry using traditional methods.

Scarborough Reef (Fig. 1c) is situated 296 km east of Zhongsha Islands and 198 km west of Subic Bay, the Philippines. It has an isosceles right triangle shape with an area of 130 km^2 and depths at 10 to 20 m inside the lagoon. It is formed by coral reefs and coral rocks that emerge at high tide, and thus plays a key role in the strategic position in the SCS. Besides, the reef and its surrounding ocean are popular fishing grounds that result in severe sovereignty issues between the neighboring countries. Alison Reef (Fig. 1d) is an ellipse-shaped coral atoll located in the Spratly Islands, south of SCS. It is the second largest atoll in the Spratly Islands, with a width of 7.4 km, an area of 72.5 km^2, and a peripheral length of 20 km.

Bombay Reef (also known as Langhua Jiao, Fig. 1e) is the ellipse-shaped atoll located in Paracel Islands. The size of Bombay Reef is around 17 km long and 5 km wide with an area of 70 km^2. It consists of sandbars and coral reefs. Barque Canada Reef (Fig. 1f) with a long fusiform shape and with a lagoon inside is the largest island (66.4 km^2) in the Spratly Islands. The length of the island is 28 km in northeasterly direction and 1 to 4 km in east–west direction. Barque Canada Reef has sufficient area for construction, and hence several manmade infrastructures and buildings can be identified in the high-resolution satellite images. Finally, Investigator Shoal (Fig. 1g) is an intermittent coral

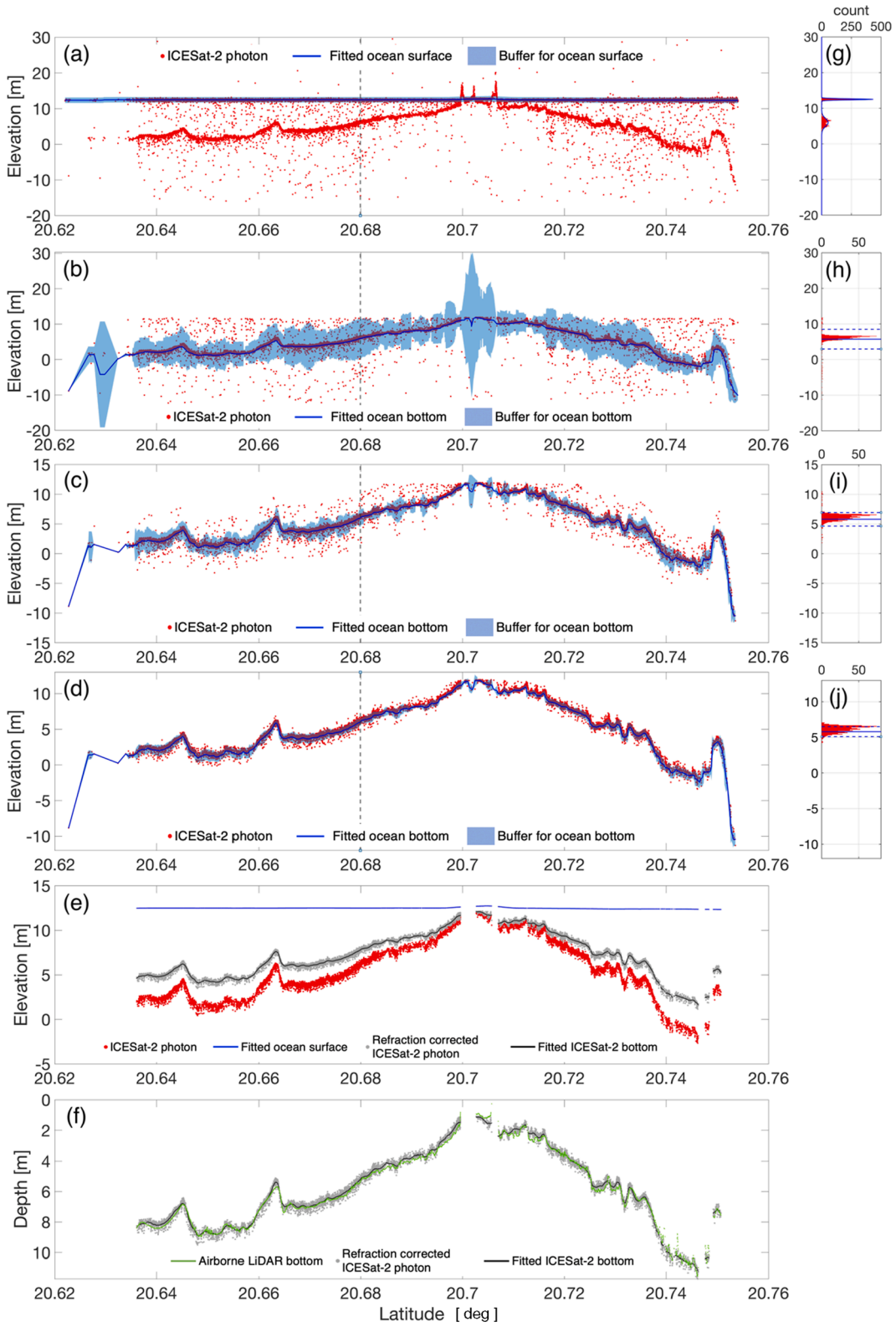

Fig. 3. An example of point cloud filtering by ICESat-2 beam 3L on 2019/01/29 in Dongsha area. (a) Original point cloud (red) and the $\mu_1 \pm 3\sigma_1$ range of the detected sea surface (blue shade). (b) Ocean floor fitting after sea surface removal. Blue shade indicates the 2σ buffer zone of the first round of median filtering. (c) Blue shade indicates the 2σ buffer zone of the second round of median filtering. (d) Blue shade indicates the 2σ buffer zone of the third round of median filtering. (e) Refraction correction based on the sea surface (blue line) in panel (a) is applied to adjust the overestimated water depth. Red points are before correction and gray points are after correction. Black line is the running mean of 30 m segment. (f) Transformation of datum from ellipsoidal height to water depth relative to the mean sea surface. Green dots display the ground truth. Panel (g–j) is a sample histogram of its left panel at 20.68° in latitude. Photon distribution (red) is aggregated in ±1,000 m (Panel g) or ±200 m (Panel h–j) with 0.1 m vertical bin size. (g) Blue curve is the two-degree Gaussian fitting. (h–j) Blue line is the median and blue dashed line is the 2σ buffer zone. (For interpretation of the references to color in this figure legend, the reader is referred to the web version of this article.)

reef of the Spratly Islands, which consists of Erjiao Jiao, Langkou Jiao and Juantou Jiao. The length of Investigator Shoal is 34 km long with 14 km wide. The lagoon depth inside Investigator Shoal is about 5.4–18.2 m.

For each site, a mask is generated by visual delineation of the outmost (furthest) underwater features in satellite images. An extra 200 m buffer towards the seaside is used to automatically select ICESat-2 candidate points within the study site.

2.2. Workflow

The present work first extracts precise ICESat-2 measurements of water depth in coastal areas, and then uses these limited height profiles to train Sentinel-2 multispectral image for a full coverage of water depth. A detailed workflow for operational purposes is shown in Fig. 2. For each target island, the ICESat-2 point cloud and Sentinel-2 images are spatially searched. It is assumed that the islands mostly formed by coral reefs would have exhibited very slow morphology (Masselink et al., 2020) and thus the vertical change is ignorable within the study period (2018–2019). ICESat-2 georeferenced photon heights from the ATL03 data product (Neumann et al., 2020) are processed with a multi-peak Gaussian fitting procedure to filter out ocean surface, followed by three iterations of a median filter to locate the bottom surface from the photon cloud. If the quality of photon height points along each of laser beams was free of identified issues stated in the technical documents, these points would be randomly split into training (90%) and validation (10%) datasets. For Sentinel-2, the Multispectral Instrument (MSI) images (Drusch et al., 2012; Gascon et al., 2017) are preprocessed by the Second Simulation of a Satellite Signal in the Solar Spectrum (6S) radiative transfer code (Vermote et al., 1997). Sentinel-2 images are spatially interpolated by ICESat-2 points to develop three empirical models, namely the Modified Linear/Polynomial/Exponential Ratio Models (MLR, MPR, MER), with their kernel variables formed by the log-ratio between the green and blue bands (Stumpf et al., 2003). Once the goodness-of-fit (GoF) is qualified by a predefined threshold (i.e., 2 m), the entire image is utilized to calculate water depth by using the model solved from the training stage. Sorted candidates of Sentinel-2 images would enter the last step to calculate the weighted average of gridded SDB product. Finally, an independent dataset from either ICESat-2 or other *in-situ* data with higher accuracy is used for validation.

3. Data and methods

3.1. ICESat-2 ATL03 data

ICESat-2 measures the range to the surface at 10 kHz repetition frequency (~70 cm sampling distance) with three pairs of 532 nm green laser beams (90 m between a dual set and 3.3 km between pairs). The Global Geolocated Photon Data (ATL03) Version 2 (Neumann et al., 2019a; Neumann et al., 2019c; Neumann et al., 2020) provides necessary geophysical corrections, including solid earth tides, ocean loading, solid earth pole tide, ocean pole tide, and total column atmospheric correction. As of October 2019, there were 8 overpasses available near Dongsha area. However, it is noted that several issues affecting the quality of ATL03 surface measurement were identified, such as the presence of clouds, multiple telemetry bands, and apparent multiple surface returns (Neumann et al., 2019b). By taking a preview of these files, only two (2019/01/29 and 2019/04/30) out of 8 files contained useable height profiles without cloud-cover issue. For each file, the longitude, latitude, and height of each data point from all six beams are extracted.

To find the ocean surface and the seafloor from point clouds, we apply the following filters with different spatial windows to remove photon events reflected from the surface, within water, or other noises apparently present below the seafloor. Using one of the beams collected on 2019/01/29 as an example, Fig. 3 visualizes the results from each of these steps.

(Step 1) Ocean Surface Detection

An aggregation distance of ±1,000 m (W0) along the satellite flight path is first applied to collect photons from ATL03 point clouds with a 70-cm progressive step (Fig. 3a). This is to form a histogram of elevation distribution to find the ocean surface. The vertical bin size v in the histogram is chosen according to the Sturges' formula (Sturges, 1926):

$$v = \frac{D}{1 + \log_2 n} \tag{1}$$

where D is the vertical range and n is the number of samples.

Since the vertical range of variation within the aggregation window, either for sea surface points or the following ocean floor points, is about 1 m, the bin size v for ~ 500 aggregated points in this spatial window is 0.1 m. Next, a two-degree Gaussian distribution is applied to fit the histogram (Fig. 3g). Assuming the combined variation of surface waves and surface gradient is gradual (submeter level) within the moving window, the surface points would form a clear Gaussian peak in the height histogram (see Fig. 3g as exemplified by a moving window near 20.68° in latitude). Thus, a considerable number of photons within the spatial segment could form a double-peak histogram, with a primary crest near the sea surface and a secondary crest near the seafloor. The two-degree Gaussian model h is as follows (Eq. (2)):

$$h = \alpha_1 e^{\left(-\frac{(x-\mu_1)^2}{{\sigma_1}^2}\right)} + \alpha_2 e^{\left(-\frac{(x-\mu_2)^2}{{\sigma_2}^2}\right)} \tag{2}$$

where α_1 and α_2 are the amplitudes, μ_1 and μ_1 are the expectations, and σ_1 and σ_2 are the standard deviation of each crest, respectively.

The first peak is assumed to be the ocean surface. A demonstration of $\mu_1 \pm 3\sigma_1$ is displayed by the blue shade in Fig. 3a. Photon events falling within this window are considered as surface returns and removed in this stage. The photons located higher than this height band are also eliminated. It is noted that this surface will be later used as the penetration surface for refraction correction in Step 3.

(Step 2) Seafloor Detection

Since the reflected photons experiencing volume scattering exhibit a high-amplitude fluctuation in contrast to the relatively smooth bottom terrain, an iterative moving window can detect the seafloor where most photons are reflected. For the photon events preserved from Step 1, a new aggregation distance of ±200 m (W1) is used to remove photon events randomly scattered in volume and apparently deviating from the "long-wavelength" formation of seafloor. In this step, a median filter is adopted instead of a mean filter because of the skewed distribution of height histogram. The photons appear mostly in the lower part of height histogram under the low turbidity condition. The surface found by this step is shown in Fig. 3b with a buffer zone of 2σ. The points outside this height band are then removed. The same median filter (W1) iterates two more time to remove photons deviated from the main group, as shown in Fig. 3c–d. Finally, a moving average spanning ±30 m (W2) is applied to compute the height of each remaining photon, which is later referred as "photon height". To ensure height estimates are determined by sufficiently dense and repeated samples, only the windows containing at least 20% of its original point density, or > 6 points in each 30 m sector in equivalent, are used.

(Step 3) Refraction and tidal corrections

ICESat-2 photons heights in ATL03 are calculated based on the speed of light in the air. Since the speed of light reduces from 2.997×10^8 m s^{-1} in the air to 2.235×10^8 m s^{-1} in seawater (Mobley, 1995; Parrish et al., 2019), a refraction correction is needed to adjust the over-estimated water depth. The corresponding refractive indices in Eq. (3) are 1.00029 and 1.34116 for air (n_a) and seawater (n_w), respectively. Here, we define the original depth Z_O as the difference between the photon height estimated in Step 2 and the corresponding sea surface height fitted in Step 1. After the refraction correction shown in Eq. (3) (Green et al., 2000; Parrish et al., 2019), the new water depth Z_n would

be shallower than the original water depth (see gray dots in Fig. 3e).

$$Z_n = Z_O * \left(\frac{n_a}{n_w}\right) \quad (3)$$

where Z_n is the new depth, Z_O is the original depth, and n_a and n_w are the refractive index in air and in seawater, respectively.

Theoretically, the incidence angle of ICESat-2 beams would cause a bending of light in water and associated geolocation changes. However, because of a very small off-nadir angle limited to 1.8° (Neuenschwander et al., 2019) during the entire mission (up to 0.46° in Dongsha's beam 3L on 2019/01/29), the emitted beams induce as large as 9 cm of horizontal offset at a depth of 30 m due to refraction (Parrish et al., 2019). Compared to the laser footprint (10.9 m ± 2.1 m) (Prof. L. Magruder, personal communication, Oct 20, 2020), the pointing accuracy (~6.5 m), and the Sentinel-2's GSD (10 m), the horizontal shift due to the refraction of seawater is small enough to be ignored in the computation. Finally, the tidal correction referred to DTU16 (Technical University of Denmark tide model) is applied to transfer the datum from an elevation-oriented WGS84 to the depth-oriented DTU16 mean sea surface (MSS) (Fig. 3f).

3.2. Sentinel-2 MSI level 1 data

Sentinel-2A and 2B were launched in June 2015 and March 2017, respectively. Each of them carries the Multispectral Instrument (MSI) that offers 10 m resolution images in every 10 days. (Drusch et al., 2012). All Level-1C orthorectified Top-of-Atmosphere (TOA) granules covering target islands with cloud-coverage<10% are downloaded through the Copernicus Open Access Hub (https://scihub.copernicus.eu). The images over Dongsha are firstly tested by two kinds of atmospheric correction to examine the individual performance, including the *sen2cor* (Dongsha Islands only) and 6S algorithms (all islands). The *sen2cor* module in the Sentinel Application Platform (SNAP) software utilizes a library inherited from the Atmospheric and Topographic Correction (ATCOR) of the German Aerospace Center (DLR) and a set of look-up tables generated via the Library for Radiative Transfer (LibRadtran) for calculating solar and thermal radiation in the Earth's atmosphere (Louis et al., 2016). On the other hand, the Python interface to the 6S Radiative Transfer Model outlined by Wilson (2013) is also tested to correct gaseous absorption and the scattering of molecules and aerosols along the light path. The absorption effects due to water vapor and merged ozone are referred to the Total Ozone Mapping Spectrometer (TOMS) and the Ozone Monitoring Instrument (OMI) observations, provided by the National Centers for Environmental Prediction (NCEP) and the National Center for Atmospheric Research (NCAR) (Kalnay et al., 1996). In addition, the scattering term such as the aerosol optical thickness at 550 nm adopts the Moderate Resolution Imaging Spectroradiometer (MODIS) Atmosphere Monthly Global product (MOD08_M3.006). Since ATCOR algorithm is a land-oriented atmospheric correction method (Gao et al., 2009), 6S had been confirmed to outperform ATCOR over water surfaces (Nazeer et al., 2014). In fact, 6S is more consistent over various of surface types (López-Serrano et al., 2016). As discussed later in Table 3, the SDB using images corrected by 6S also outperforms the ones corrected by *sen2cor*. Hence, 6S is adopted in the processing chain for the rest of five islands.

Following that, a simple union of spectral criteria is designed to remove the remaining scattered clouds from the image. Taking advantage of the spectral feature of Red and Infrared bands over clouds, these two bands display higher reflectance as compared with land, ocean, reef, sea grass, etc. After experimental iterations over all islands, a multi-band threshold is concluded that when a pixel whose Infrared band > 0.09 and Red band > 0.07 is flagged as a cloud pixel and filled by a null value. All images collected herein are corrected by the 6S model and become candidates in the following training stage.

Table 1
Summary of the empirical models used in this study. Z is the depth and R is the ratio from Eq. (4). *a*, *b*, and *c* are the parameters to be determined.

Model name	Modified Linear Ratio Model (MLR)	Modified Polynomial Ratio Model (MPR)	Modified Exponential Ratio Model (MER)
Functions	$Z = aR + b$	$Z = aR^2 + bR + c$	$Z = ae^{bR} + c$

3.3. Semi-empirical model training

ICESat-2 depth points and the collocated Sentinel-2 pixels are spatially paired up for training the spectral model with an exponential decay signature (Albright and Glennie, 2020). In the model introduced by Stumpf et al. (2003), a log ratio between the Blue and Green bands (Eq. (4)) is linearly correlated with water depth. The ratio transformation model (Eq. (4)) thus serves as the kernel of our modified version of fitting functions. It is noted that other optical band combinations could form a multiple linear regression model (Geyman and Maloof, 2019), which could provide extra ratio-attenuation information over various substrate types.

$$R = \frac{ln(n*B1)}{ln(n*B2)} \quad (4)$$

where R is the band ratio, *B1* and *B2* are the reflectance of Blue and Green bands, respectively, and *n* is a constant (1500 in this case) to ensure the positive ratio after natural logarithm transformation.

Because the linearity between *R* and depth only maintains in a certain shallow water interval and becomes non-linear afterwards (Cahalane et al., 2019), two other empirical functions are examined in this paper to fit the relationship between *R* and depth provided by ICESat-2. These three models are named the Modified Linear/Polynomial/Exponential Ratio Models, or simply MLR, MPR, and MER. The functions are shown in Table 1, in which *a*, *b*, and *c* are the parameters derived from a least-squares regression. Here, 90% of refraction-corrected ICESat-2 bathymetric points in each 1-meter vertical interval are randomly selected for training (hereafter K_{90}). The remaining 10% of points (hereafter K_{10}) are reserved as reference data in the validation stage.

4. Results

4.1. Validation of ICESat-2 sea surface height

Since the instant sea surface height (SSH) measured by ICESat-2 is a key parameter for refraction correction, it is necessary to verify the validity of SSH observation. The DTU18 MSS model (Andersen et al., 2018) released by the National Space Institute in University of Denmark (DTU space) is a global map in 1′ spatial resolution detailing the displacement of sea surface that approximates the formation of geoid (www.space.dtu.dk). DTU18 MSS is a successor of the previous version of MSS that purely incorporated satellite altimetry missions (e.g., Topex/Poseidon and Jason-1/-2) in the last two decades. It is improved with an inclusion of the latest synthetic aperture radar (SAR) altimetry missions, such as Cryosat-2 and Sentinel-3 (Andersen et al., 2018). One assumption made here is that the dynamic topography and currents only induce a constant vertical shift along this short latitudinal sector. Hence, the ICESat-2 derived sea surface (Fig. 3a), after tidal correction, can be compared with the bilinearly interpolated DTU18 at the coordinate of each photon identified as ocean surface layer and check their relative discrepancies.

In our results, ICESat-2 SSH matches well with DTU18, with a good agreement of $R^2 = 0.92$ and a low standard deviation of difference at 3.5 cm. The discrepancy is primarily attributed to the wind-driven and shoaling waves. The error budget is close to 2 cm as reported by a recent study of ICESat-2 over 30 lakes and reservoirs in China (Yuan et al.,

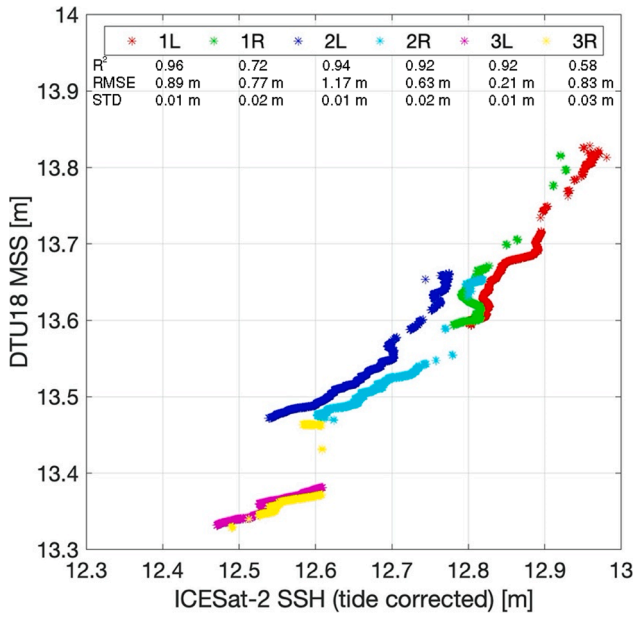

Fig. 4. Comparison between ICESat-2 derived sea surface height (SSH) and DTU18 mean sea surface (MSS) along the six beams measured on 2019/1/29. The heights are referenced to the WGS84 ellipsoid.

Table 2
Validation of ICESat-2 derived water depth in Dongsha Island from 6 ground tracks (GT).

Date	Index	Ground Track					
		1L	1R	2L	2R	3L	3R
2019 01/ 29	Number of photons	4813	825	5383	935	10,538	1324
	RMSE [m]	0.40	0.35	0.54	0.61	0.50	0.54
	RRMSE [%]	12%	22%	9%	12%	9%	11%
	STD [m]	0.27	0.13	0.18	0.14	0.17	0.13
	R^2	0.99	0.91	0.99	0.99	0.99	0.99
	Average interval [m]	3.86	21.92	3.04	14.95	1.18	8.32
2019 04/ 30	Number of photons	5587	361	4034	487	–	–
	RMSE [m]	0.26	0.32	0.36	0.49	–	–
	RRMSE [%]	4%	6%	6%	8%		
	STD [m]	0.17	0.24	0.23	0.33		
	R^2	0.97	0.94	0.99	0.97	–	–
	Average interval [m]	3.19	45.38	3.26	19.06	–	–

2020). The comparison is illustrated in Fig. 4, where different colors depict the SSH in WGS84 ellipsoidal height derived by six beams of ICESat-2 near Dongsha Island on 2019/1/29. However, it is noted that a bias of ~ 0.9 m exists in every height profile after a necessary correction for the instant tidal height of −0.13 m. The cause of this systematic error still remains elusive. We note that the DTU13 geoid given in ATL03 at the center of this segment is 12.2 m, 12.05 m, and 11.9 m for 1L, 2L, and 3L, respectively, which has also a bias of ~ 0.7 m. Nevertheless, it confirms that we could use the surface fitted from ATL03 profile instead of a flat-surface simplification to calculate refraction correction, to avoid errors in a few tens of centimeters.

4.2. Validation of ICESat-2 bathymetry with airborne LiDAR

ICESat-2 derived water depth is first compared with airborne LiDAR data in Dongsha Island (Shih et al., 2011). The comparison of each beam on two dates is summarized in Table 2, in which the number of photons is the number of photon heights calculated by a 30-m running mean at each photon, such as the last part in Step 2 of Section 3.1. The quality indicators include RMSE, STD (standard deviation of the difference,), and R^2 as compared against airborne data. The average interval is computed from the length of the transect within the island mask divided by the number of photons, as an indicator of the "sampling distance" under the mixed environmental conditions.

The RMSE between two datasets ranges from 0.26 m to 0.61 m, while the STD values range from 0.13 m to 0.33 m and R^2 values range between 0.86 and 0.99 for all 10 beams on both dates. The difference between RMSE and STD is presumably due to the errors in tides and datum transformation. STD, which is about a half of RMSE, is subjected to the error in aggregation segment (W1), geolocation error, and surface fitting/modeling (W2) error. Generally, strong beams perform better than weak beams in terms of RMSE (4 out of 5 pairs) and R^2 (5 out of 5 pairs). Strong beams also have a shorter average interval (except for GT1 L/R on 2019/01/29) owing to their greater penetration capability. The relative RMSE (RRMSE) in Table 2 is defined as RMSE divided by the average depth in the transect, indicating the percentage of error as normalized by the depth those photons could reach. Nevertheless, all the beams achieve an unprecedented accuracy to measure shallow water depth that can serve as training and validation datasets for other spaceborne sensors.

4.3. ICESat-2 trained Sentinel-2 SDB

Since the quality of bottom-of-atmosphere (BOA) reflectance corrected by SNAP *sen2cor* or 6S may not be completely reliable due to the unfavored surface conditions such as cloud shadow, sun glint, and waves, it is difficult to select a single image to derive water depth. Moreover, the unknown water quality and the diffusive coefficient for

Table 3
Comparisons of GoF during the training stage and the RMSE in validation stage, by using the 9–1 split of ICESat-2 depth points in Dongsha Island. The format is GoF/Validation (in terms of RMSE) in meter. The RMSE better than 1 m is highlighted to show the outperformance of 6S corrected images.

Sentinel-2 Date	MER		MLR		MPR		
	sen2cor	6S	sen2cor	6S	sen2cor	6S	RRMSE
2018/03/05	1.26/1.16	0.87/**0.82**	1.43/1.24	0.87/**0.82**	1.23/1.15	0.86/**0.82**	15%
2018/04/04	1.17/1.10	0.85/**0.81**	1.21/1.10	0.89/**0.83**	1.17/1.10	0.85/**0.81**	15%
2018/04/14	1.46/1.37	1.11/1.05	1.50/1.38	1.08/1.03	1.45/1.38	1.08/1.03	19%
2018/05/05	1.72/1.61	1.41/1.35	1.73/1.60	1.39/1.33	1.69/1.57	1.37/1.30	24%
2018/07/08	1.28/1.10	1.19/1.03	1.30/1.10	1.14/1.00	1.21/1.02	1.09/**0.95**	18%
2018/07/28	1.13/1.02	1.04/**0.95**	1.18/1.05	1.01/**0.93**	1.13/1.02	1.01/**0.92**	17%
2018/09/06	0.91/**0.88**	0.86/**0.84**	0.94/**0.88**	0.84/**0.83**	0.90/**0.87**	0.84/**0.83**	16%
2018/09/26	1.38/1.27	1.32/1.17	1.41/1.27	1.25/1.13	1.38/1.27	1.25/1.13	21%
2018/10/06	0.75/**0.69**	0.69/**0.64**	0.88/**0.76**	0.70/**0.64**	0.75/**0.69**	0.69/**0.64**	12%
2018/10/26	1.35/1.26	1.21/1.13	1.39/1.28	1.18/1.11	1.35/1.25	1.17/1.10	21%
2019/02/03	0.95/**0.89**	0.78/**0.77**	1.04/**0.91**	0.76/**0.74**	0.93/**0.89**	0.76/**0.73**	14%
2019/02/23	1.39/1.32	1.29/1.21	1.40/1.34	1.26/1.20	1.38/1.32	1.26/1.20	23%

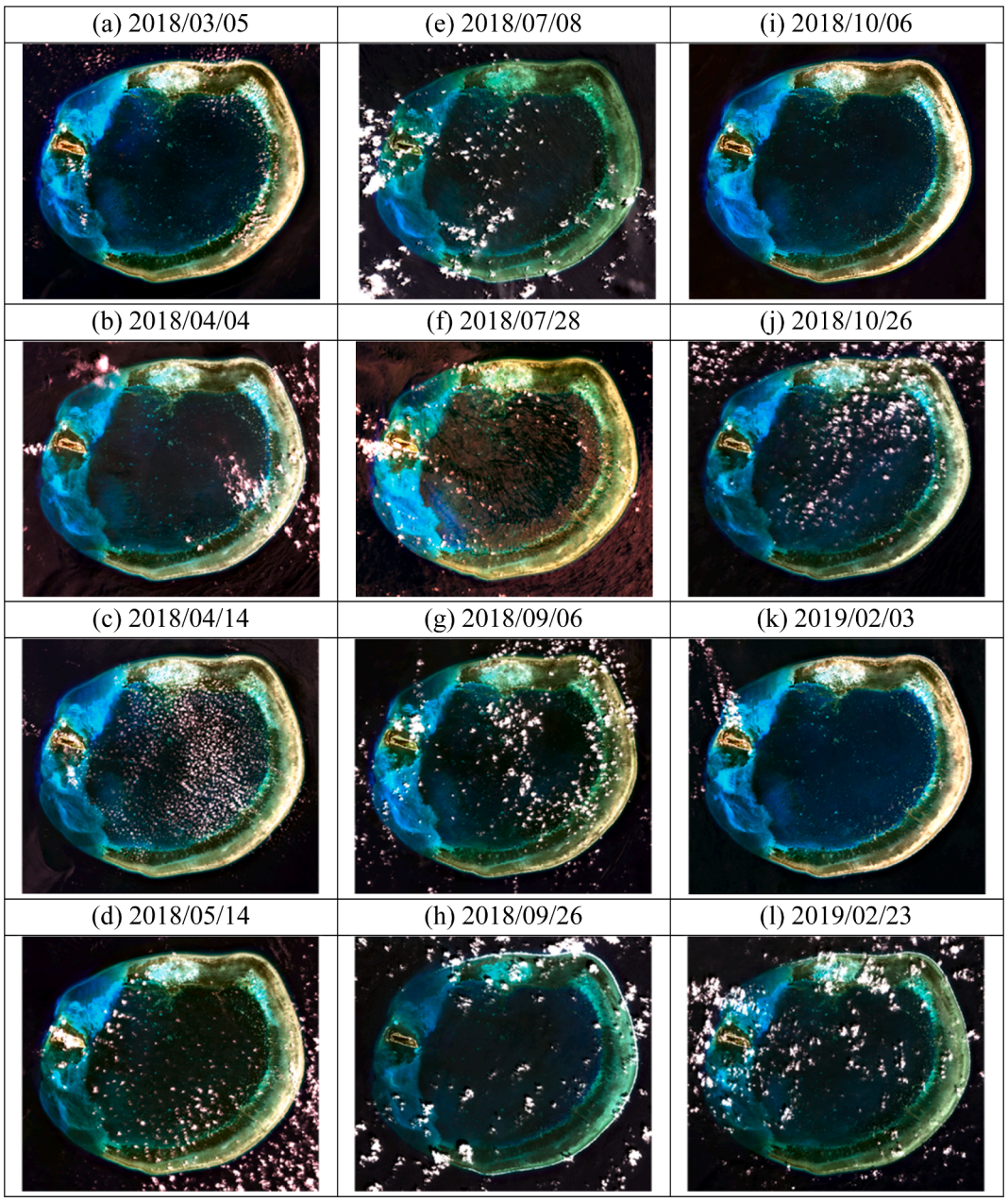

Fig. 5. True color images composed from Sentinel-2 images (R/G/B: Band 4/3/2).

each particular island at certain time are difficult to estimate. Thanks to the 5-days revisit of Sentinel-2A/B, a number of images can be selected during the study period. In Dongsha Island, a total of 12 image candidates with $<$ 10% cloud collected between March 2018 and February 2019 is demonstrated in Fig. 5. This set of true-color images is comprised of different solar, atmospheric, and ocean surface conditions. Therefore, the image selection procedure is important to ensure the quality of SDB products.

Without applying more sophisticated image correction procedures, a simplified approach is introduced here by using the fitting model to determine the quality and applicability of an image based on the statistical performance. The fitting results are demonstrated in Fig. 6, and the coefficients a, b, and c in Table 1 are derived from the least-squares regression.

The trend of scattered points, although visually linear in the depth of 4–10 m, starts to diverge between fitting models when the water depth is outside this range. As observed in Fig. 6, the higher order terms in MPR are sensitive to the distribution of scattered training points over 10 m, and make the fitting curve drastically down-turned especially for those images with complex atmospheric and surface conditions. However, it should be emphasized that the following validation is only conducted within 20 m by using airborne LiDAR data in Dongsha, or within 15 m by 10% of ICESat-2 data split (K_{10}) in all six islands. Some extremely large errors in deep water can be expected from those models with large fitting errors but not shown in this study.

The fitted model is then applied to all pixels in the same Sentinel-2 image. The pixel would be assigned a null value when the modeled depth is negative (above ocean surface). A set of bathymetry maps from MER, which is quite similar to the other two models, is demonstrated in Fig. 7. The water depths derived from different images seem to be similar in the shallow water ($<$5 m) part. The major uncertainty across these 12 images appears in the lagoon, with apparent variation from 8 m to$>$20 m deep. This is because MER, and other models, have larger uncertainty for deep water ($>$10 m) as compared to shallow water

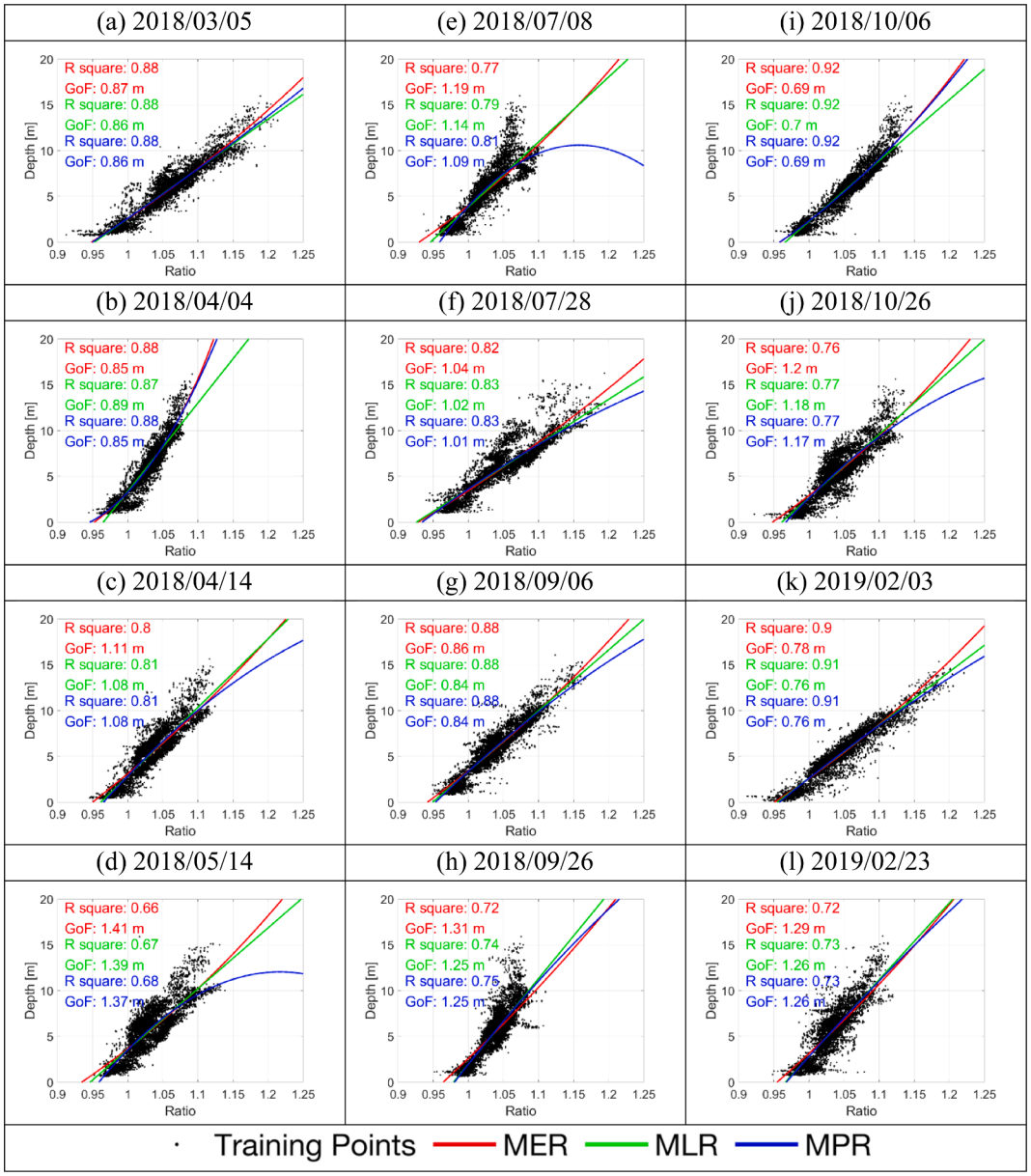

Fig. 6. Fitting results of Sentinel-2 images in Fig. 5. In each panel, y-axis is ICESat-2 derived depth Z and x-axis is the ratio R of the corresponding Sentinel-2 pixel.

(Fig. 6). The scattered points in deep water can be attributed to different ocean surface conditions, the residual of atmospheric contamination, various attenuation coefficients, and/or the maximum light penetration. Without knowing the quality of an image in this way, it is difficult to assess the quality of the derived bathymetry. It can be found in a narrower spread of scatter points in the fitting procedure (Fig. 6), such as images on 2018/03/05, 2018/04/04, 2018/09/06, 2018/10/06, and 2019/02/03, the SDB presents a better quality and a clearer gradient pattern, especially in the deep region (>10 m). Therefore, in the following sections we develop a fusion scheme to include useful images and reject images compromised by the abovementioned quality issues. These criteria substantially reduce the scatter in SDB, and produce a much narrower spread of scatter points in the fitting procedure.

To quantify the quality of selected images in the pool for SDB production, the goodness-of-fit (GoF) parameter is an appropriate indicator to evaluate the model during the training stage. GoF is directly linked to the quality of depth estimated by an image, which is also an inference of image quality and a prediction of depth accuracy. The computation of GoF follows Eq. (5), where $z(i) - \hat{z}(i)$ is the residual of depth points from the fit (model) to the photon height at ith location, K_{90} is the number of 90% ICESat-2 points used for training, and m is the number of fitted coefficients. The computation of RMSE for validation follows Eq. (6), in which $z(j) - \hat{z}(j)$ is the residual of depth points from the fit $z(j)$ to the 10% of ICESat-2 points at jth location, and K_{10} is the number of preserved 10% ICESat-2 points.

$$GoF = \sqrt{\frac{\sum_{i=1}^{K_{90}} (z(i) - \hat{z}(i))^2}{K_{90} - m}} \tag{5}$$

$$RMSE = \sqrt{\frac{\sum_{j=1}^{K_{10}} (z(j) - \hat{z}(j))^2}{K_{10}}} \tag{6}$$

A comparison between GoF and Validation results confirms the coherence over all the examined models and images, with a correlation of 0.99 and a standard deviation of the difference at 0.04 m for all cases. As summarized in Table 3, GoF and RMSE values during the training and

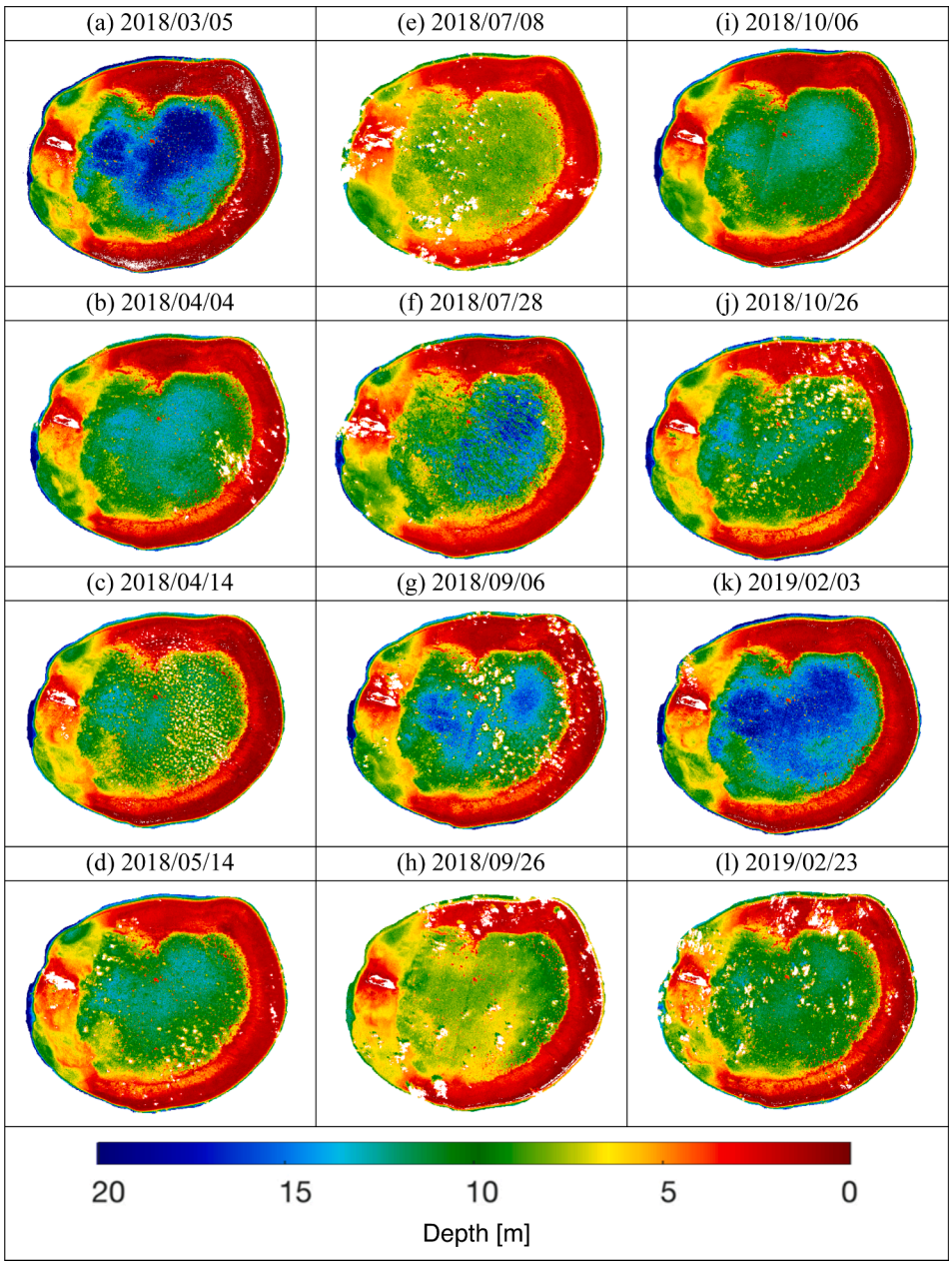

Fig. 7. Satellite Derived Bathymetry (SDB) produced by Sentinel-2 images and ICESat-2 training points.

validation stage imply that the error of the SDB product is predictable during the model fitting stage. This is particularly important when the valid ICESat-2 ATL03 points are scarce for a small island, where the validation set has very limited number of points. Table 3 also shows that images corrected by 6S model outperform the same ones corrected by *sen2cor* algorithm in all validation cases. The SDB products with accuracy better than 1 m (highlighted in bold) are more in 6S corrected images. Hence, we only use 6S correction for the other five islands. In addition, the relative RMSE (RRMSE) in the last column is calculated by dividing "MPR 6S Validation" with the average depth, showing the percentage of error is about 12%–24% of the depth.

During the study period, the number of clear images is 12 for Dongsha Island, 8 for Scarborough Reef, 14 for Alison Reef, 7 for Bombay Reef, 2 for Barque Canada Reef, and 4 for Investigator Shoal. The same workflow developed from Dongsha's case is applied to all other ICESat-2 beams and 47 Sentinel-2 images in an automatic manner. The results of the three models are exemplified by one of the images (Fig. 8). The uncertainty of SDB derived from different models is also, although not obvious as Fig. 8 shows, mainly in the deep zone (>10 m). The estimates in deep area depend on the higher order terms in MER and MPR.

4.4. Increasing SDB quality from redundant observations

In the same way, GoF and Validation results given by three models for those 47 images are obtained. However, to fully exploit the advantage of repeating satellite images, a combination of multiple images is presumably more accurate and reliable than the single one. The accuracy should be improved with repetitive observations whilst only random error exists. Hence, a weighted average is applied here for the images and check whether the accuracy can be further improved. This step not only produces a new SDB product to reduce potential random noise existed in either of the images, but also can help to fill the null pixels due to cloud contaminations and/or modeling errors. The formula

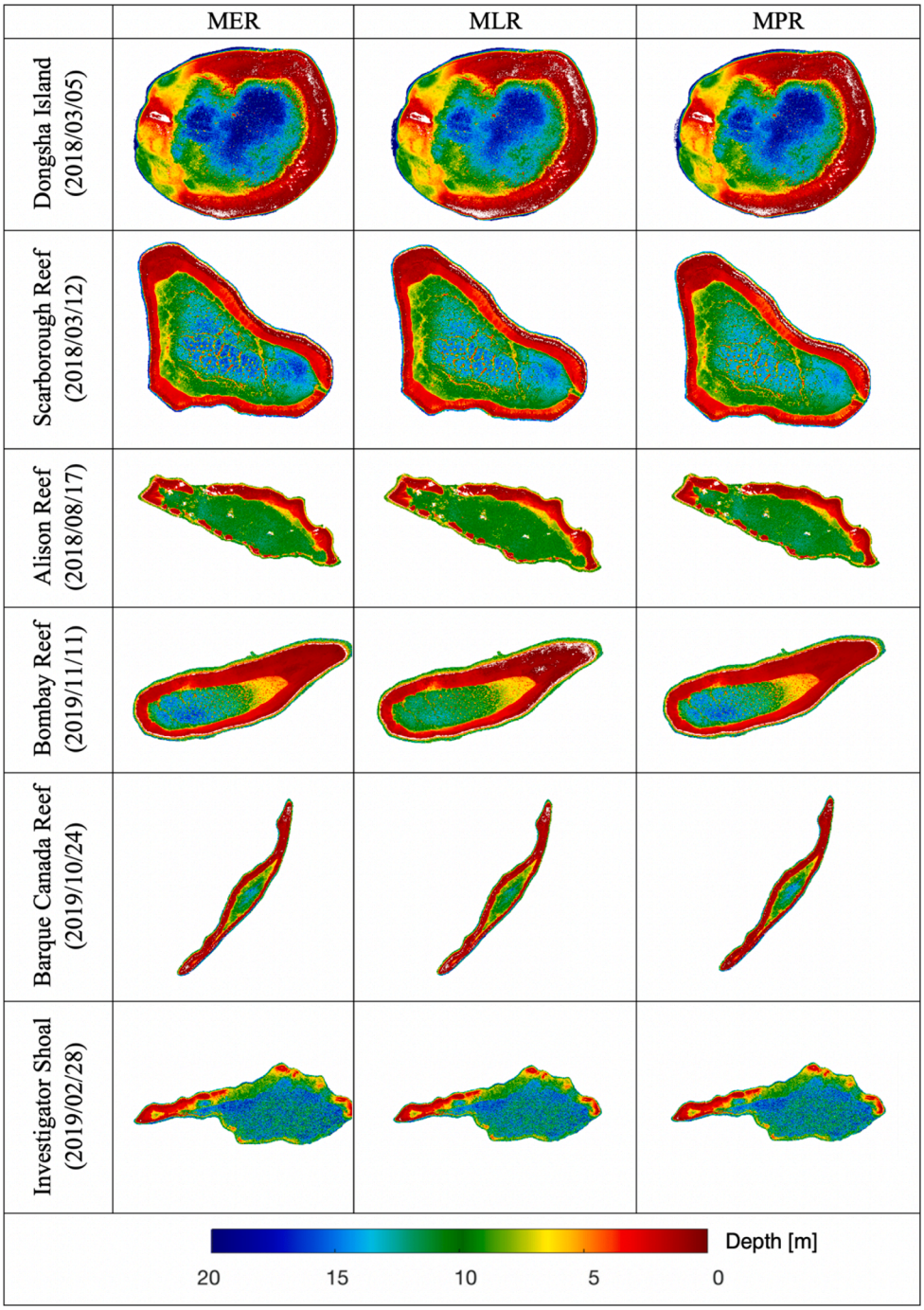

Fig. 8. Satellite Derived Bathymetry (SDB) results in 6 target islands using three semi-empirical models.

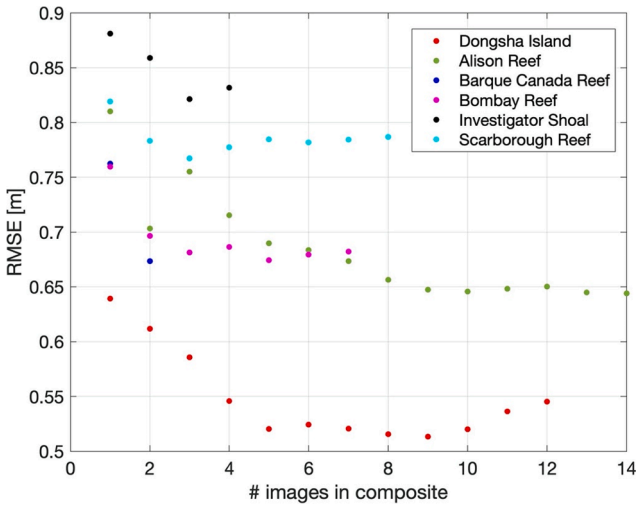

Fig. 9. Root-mean-square error (RMSE) of the composite image as a function of number of images in the composite.

used to calculate the weighted-average SDB is shown in Eq. (7), where Z_c is the composite image through weighted average, Z_l is the depth map given by any single image in the pool, l is the number of aggregated images, n is the maximum number of images in that island, and σ_l is the *a priori* accuracy estimated from GoF values.

$$Z_c = \left(\sum_{l=1}^{n} \frac{1}{\sigma_l^2} Z_l\right) \times \left(\sum_{l=1}^{n} \frac{1}{\sigma_l^2}\right)^{-1} \tag{7}$$

It should be mentioned that the images in the pool have been sorted in the descending order of accuracy. Hence, it can be expected that the weighted average from the first few images would produce a better result than using the entire dataset. In other words, the subsequent image whose GoF is slightly worse may introduce extra "outliers" in the earlier composite due to the poor quality of some particular pixels. Therefore, the maximum number of aggregated images ($\hat{n}$) should be optimized based on the following condition:

$$\hat{n} = \underset{n}{arg\min} \left(\sqrt{\frac{\sum_{j=1}^{K_{10}} (Z_c(j) - \hat{z}(j))^2}{K_{10}}} \right) \tag{8}$$

where $\hat{n}$ is the optimized number of images in use, $\hat{z}(j)$ is the 10% of ICESat-2 validation point, $Z_c(j)$ is the interpolated depth at j^{th} location in composite Z_c.

Hence, the optimized composite image can be formed as Eq. (9):

$$\hat{Z}_c = \left(\sum_{l=1}^{\hat{n}} \frac{1}{\sigma_l^2} Z_l\right) \times \left(\sum_{l=1}^{\hat{n}} \frac{1}{\sigma_l^2}\right)^{-1} \tag{9}$$

As shown in Eq. (7), the composite image keeps updated as the increasing number of images in use. In the meantime, the RMSE could be verified instantly by Eq. (8) and the optimal number of images in the composite could be determined at the minimum. It is observed that for most of islands, the inclusion of second and third image could generally reduce the error at 0.05–0.1 m level (except for a rebound of Alison Reef). Fig. 9 shows the variation of MPR RMSE in six islands as the increasing number of images in the composite. Most RMSE level starts to converge after 3–4 images in the composite, and the total reduction of RMSE at $\hat{n}$ in each case is at around 0.16 m (Alison Reef) to 0.1 m (others).

SDB derived from the optimized composite image in these six islands are verified with the independent 10% of ICESat-2 validation set. In contrast to the single image (best or second) whose RMSE is generally 0.64–1.09 m, the weighted-average SDB performs better than the best one in all cases, regardless of the number of images available. As displayed in Table 4, the RMSE values of the Best/Second/ $\hat{n}$ Weighted-Average results are compared. Even though the overall performance of MPR is slightly better than others, the difference among the three models are quite marginal. The next step is to check whether the error budget can satisfy the requirement in ZOC and their details in different water depth intervals.

4.5. Potential ZOC category of Sentinel-2 SDB

As defined by the International Hydrographic Organization (IHO), the quality of nautical charts can be categorized based on the age, position/depth accuracy, reliability, and seafloor coverage of surveying techniques (Weintrit, 2018). The Category Zone of Confidence (ZOC) system in ENC is a guideline for mariners to manage the level of risk when sailing in a certain mapped area, and to ensure a safe under-keel clearance in shallow water. In each of the five ZOC levels, the depth accuracy is a function of base error plus a percentage of error proportional to the depth. For example, the highest level *A1* requires a vertical accuracy at 0.50 m + 1% of depth and a positional accuracy at 5 m + 5% of depth, while the lower level *C* requires a vertical accuracy at 2 m + 5% of depth and a positional accuracy at 500 m. Although the current ZOC categories are standardized based on the utilization of echosounder/sonar surveys, the position and depth accuracy could be fulfilled by SDB products from various approaches, such as the multiple linear regression of log-transformed bands with Cubesat (Poursanidis et al., 2019), machine learning with Landsat-8 (Sagawa et al., 2019), and a combination of an empirical linear transformation, cloud masking, sun-glint correction, and pseudo-invariant features with Pleiades high-resolution images (Pike et al., 2019). In coastal areas, the level of ZOC is mostly B (30%), C (20%), D (20%), and U (25%) (IHO S67, 2017). Therefore, this study aims to leverage high quality ICESat-2 data and repeating Sentinel-2 images to develop a framework of SDB production, which ensures the error can be evaluated in islands without reference data.

We first examine the SDB derived from two single images (best and second in the sequence) in all six islands to discuss the accuracy of Sentinel-2 derived SDB in different depth intervals. In other words, the estimated depths from the best two images are grouped together and validated with ICESat-2 validation set in each interval, regardless of which island they belong to. The amount of validation point (including

Table 4
Summary of the RMSE values of all available images without considering the depth distribution. The format of each entry is Best/Second/ $\hat{n}$ Weighted-Average accuracy (RMSE) in meter. Numbers in the bracket of each entry is the number of $\hat{n}$ (left) and the relative root-mean-square error (RRMSE) (right).

Island	# images in the pool	MER	MLR	MPR
Dongsha Island	12	0.64/0.77/0.51 [5 , 10%]	0.64/0.74/0.50 [9 , 9%]	0.64/0.73/0.50 [9 , 9%]
Scarborough Reef	8	0.73/0.80/0.66 [3 , 16%]	0.72/0.77/0.65 [3 , 16%]	0.71/0.77/0.65 [3 , 16%]
Alison Reef	14	0.89/0.91/0.79 [5 , 29%]	0.82/0.89/0.76 [6 , 28%]	0.74/0.75/0.65 [14 , 24%]
Bombay Reef	7	0.75/0.85/0.70 [4 , 24%]	0.89/0.93/0.80 [4 , 28%]	0.73/0.83/0.70 [5 , 24%]
Barque Canada Reef	2	0.77/0.86/0.71 [2 , 40%]	0.85/0.89/0.76 [2 , 43%]	0.70/0.84/0.68 [2 , 39%]
Investigator Shoal	4	0.93/1.09/0.90 [3 , 16%]	0.91/1.05/0.84 [4 , 15%]	0.91/1.06/0.85 [4 , 15%]

Table 5
The amount of independent ICESat-2 validation point (K_{10}) of 6 islands in each depth. Dongsha Island has extra field data taken by airborne bathymetric LiDAR.

Island/ validation point numbers	Dongsha Island	Dongsha Island (field data)	Scarborough Reef	Alison Reef	Bombay Reef	Barque Canada Reef	Investigator Shoal	Total amount in each interval
0–1 *m*	69	49,539	1011	193	90	2129	44	53,075
1–2 *m*	429	53,987	639	755	1332	1979	207	59,328
2–3 *m*	205	27,273	686	120	1065	235	194	29,778
3–4 *m*	301	11,517	1269	197	204	78	70	13,636
4–5 *m*	358	13,499	90	94	66	94	81	14,282
5–6 *m*	604	16,952	48	76	36	72	56	17,844
6–7 *m*	748	21,365	129	76	25	51	45	22,439
7–8 *m*	293	21,092	198	17	46	37	79	21,762
8–9 *m*	208	22,845	241	9	60	61	118	23,542
9–10 *m*	110	18,058	368	19	48	53	156	18,812
10–11 *m*	53	19,511	351	22	45	60	76	20,118
11–12 *m*	22	18,614	140	8	38	48	41	18,911
12–13 *m*	11	18,207	15	0	35	11	25	18,304
13–14 *m*	12	20,106	1	0	10	0	1	20,130
14–15 *m*	4	25,221	1	0	2	0	0	25,228
15–16 *m*	1	29,260	0	0	0	0	0	29,261
16–17 *m*	0	21,142	0	0	0	0	0	21,142
17–18 *m*	0	6990	0	0	0	0	0	6990
18–19 *m*	0	2687	0	0	0	0	0	2687
19–20 *m*	0	1323	0	0	0	0	0	1323
Total amount in each island	3428	419,188	5187	1586	3102	4908	1193	

airborne LiDAR and independent ICESat-2 point cloud) in each depth of all 6 islands is listed in Table 5. The number of validation points from Dongsha's field LiDAR data is more evenly distributed than others from ICESat-2 validation set.

It should be emphasized that the error discussed here with ZOC is 1.96 × RMSE, because ZOC is defined by a 95% Confidence interval (CI). It is also noted that category *A2* and B have the same vertical but different horizontal accuracy requirement. In our analysis, the shallower part (<8 m) of all islands has a median of RMSE stay below or around the upper limit of ZOC category *C*. For most of depth estimates over 9 m, the median values are generally outside category *C*. The accuracy is very difficult to satisfy category *C* in most cases when the depth exceeds 16 m. As shown in subplots of Fig. 10, a box plot is used to demonstrate the distribution of 1.96 × RMSE with a 1-m depth interval for each of regression models from (a) MER, (b) MLR, (c) MPR, and (d) all the three models. Three reference lines depict the upper bound of category *C* (2 m + 5% depth, gray), category *A2* and *B* (1 m + 2%, green), and category *A1* (0.5 m + 1%, orange) in the ZOC requirement. For the box plot in each 1-m interval, the blue box displays the first and third quartile of RMSE for six examined islands, with the median colored in red. Black whisker displays the best and worst case in any of six islands' two images excluding any outliers. Red crosses appearing in some intervals are the outliers. While evaluating the models separately (panels a–c), RMSE values reasonably become larger with the increase of water depth in three models. Panel *d* summarizes the performance from all possible fitting models used in this study.

Next, the validation is conducted for the weighted-average SDB in all 6 islands. From both internal (ICESat-2, K_{10}) and external (airborne LiDAR) checks of the accuracy, the quality of SDB in Dongsha Island satisfies the requirement of category *C* within 11 m. The RMSE of weighted-average SDB of 6 islands as validated with ICESat-2 point clouds generally fulfills the category *A2* and *B* within 2 m depth and category *C* in 3–4 m interval. Fig. 11 illustrates the RMSE in each depth of 6 islands, where blue stars depict the validation by airborne LiDAR in Dongsha, and colored circles indicate the validation of each island by the 10% of ICESat-2 points. The black circle demonstrates an average of all 6 islands' accuracy validated by ICESat-2 only. We observe that Dongsha, Investigator Shoal, and Scarborough Reef can satisfy category *C* up to 8 m. Investigator Shoal and Scarborough Reef can even stay within category *C* in 13–14 m.

In summary, our accuracy of ICESat-2 photon heights (0.26 m to 0.61 m) is similar to Parrish et al. (2019) that showed RMSE at 0.43–0.60 m and Ma et al., (2020) that presented < 0.5 m errors near Yongle Atoll, SCS. For Sentinel-2 SDB, our RMSE is around 0.64–1.09 m from single image approach, and the error could be further reduced to 0.50–0.90 m with weighted-average composites. The results are improved from 0.85 to 1.85 m error level in Ma et al. (2020) and 1.03 m (95th percentile) RMSE in Albright and Glennie (2020), who also used Sentinel-2 images. Our results are comparable to Gabr et al. (2020) that obtain an accuracy at 0.38–0.43 (depth up to 8.37 m) by Planetscope and Landsat-8 images near the Northern coast of Egypt.

5. Discussion of error budget

5.1. Spatial window for point cloud aggregation

In Section 3.1, ICESat-2 point clouds are filtered by a series of spatial window to find the ocean floor. The size of window and the number of iterations are further tested here to discuss their sensitivity to the results. We compare 660 scenarios and compared the result of ICESat-2 seafloor profiles (10 ground tracks in two dates) against airborne LiDAR data in Dongsha Island. The variables in filtering process, including the aggregation segment (W1) for data filtering, iteration times, and the final window size for surface fitting (W2) are cross-combined in Fig. 12. The options of variables are listed in Table 6. In panels (a–c) of Fig. 12, the window size for iterations (W1) is chosen from ±1000 m to ±50 m (11 intervals in total) for point cloud filtering. Different colors indicate the iteration times in each test run. In each W1 interval, points from left to right are the window size (W2) used for surface fitting, varying from ±100 m to 0 m (12 options).

The general trend of all test runs shows that the correlation increases while W1 decreases from 1000 m to around 100–400 m (panel a). This range implies that the seafloor features are mainly in the wavelength of a few to several hundreds of meters. The aggregation of points over a long arc would decrease the capability of outlier removal for a section of interest. Meanwhile, the colors show that the filtering process starts to converge after three times of iterations (blue). The errors, in terms of RMSE in panel (b), drop from around 1 m (red) to around 0.5 m (green) after three times of $\pm 2\sigma$ outlier removal. However, it is not recommended to iterate more times because the spatial sampling distance, as calculated from the number of remaining points divided by the entire transect, decreases from around 5.5 m (blue in panel c) to>6 m (magenta in panel c). Therefore, to fine-tune the variable used in Step 2 of Section 3.1, the current setting is a tradeoff between accuracy and

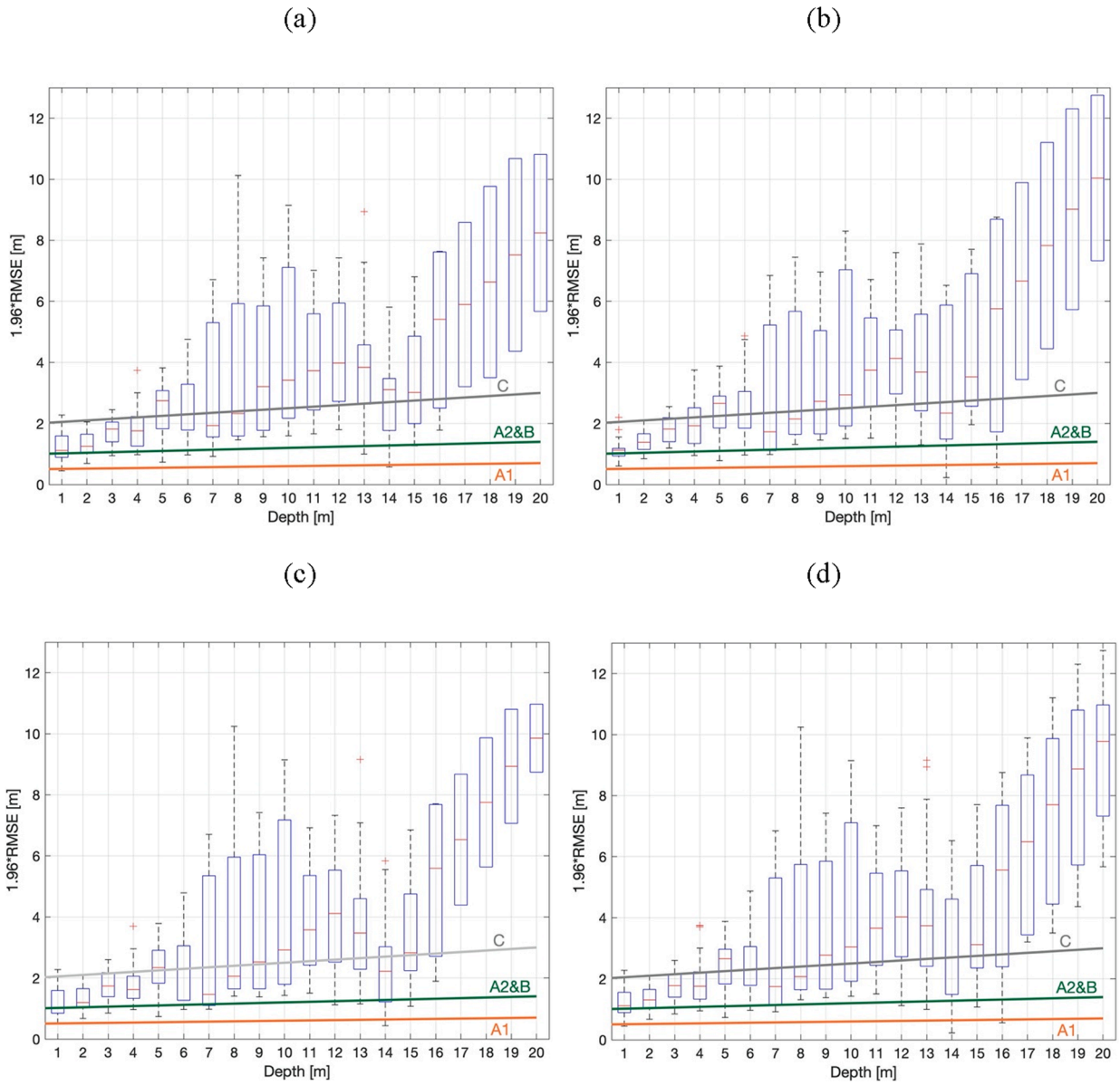

Fig. 10. Validation of accuracy of the best two single images for all six islands with a 1-m step by: (a) MER, (b) MLR, (c) MPR, (d) all three models. Gray, dark-green, orange dashed lines are the ZOC category *C* (2 m + 5% depth), category *A2* and *B* (1 m + 2% depth), and category *A1* (0.5 m + 1% depth), respectively. The depth results deeper than 15 m are only validated against airborne LiDAR data. Gray, green, and orange lines are the upper bound of ZOC category *C* (2 m + 5% depth), *A2* & *B* (1 m + 2%), and *A1* (0.5 m + 1%), respectively. (For interpretation of the references to color in this figure legend, the reader is referred to the web version of this article.)

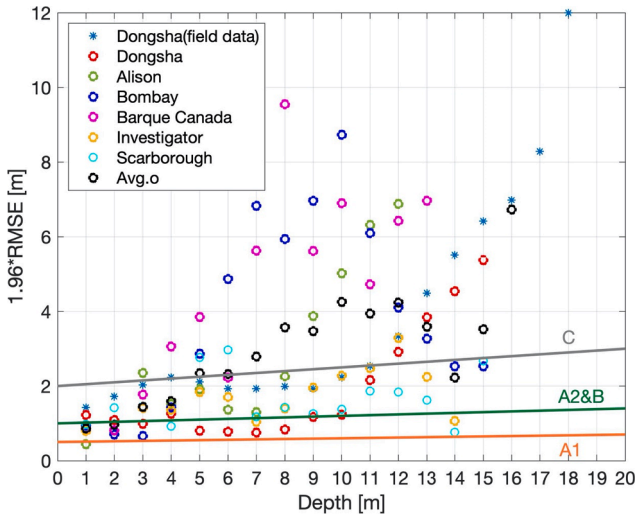

Fig. 11. Accuracy assessment of the best weighted-average SDB among three models for each of 6 islands. Depth estimates are validated in 1-m step with ICESat-2 10% validation dataset (colored circles), and with airborne LiDAR data in Dongsha (blue stars). An average of the RMSE in each 1-m interval is displayed as the black circle. Gray, green, and orange lines are the upper bound of ZOC category C (2 m + 5% depth), A2 & B (1 m + 2%), and A1 (0.5 m + 1%), respectively. (For interpretation of the references to color in this figure legend, the reader is referred to the web version of this article.)

number of points remained in the profile. Panel (d)is a blow-up view of panel (b) in W1 = 200 m. We observe that the selection of 200 m for W1, 3 times of iterations, and 30 m for W2 is a balanced combination between accuracy, correlation, and the sampling interval. Actually, it is worth noting that the accuracy is not sensitive within this preferred combination window. The accuracy only varies in centimeters level while choosing other options of W2.

The choice of spatial window is further supported by the wavenumber analysis of terrain. The power spectral density (PSD) in two directions of Dongsha Island is depicted in Fig. 13. A break point of power near 25 m of wavelength (red dashed line) implies that the formation of ocean floor over a typical inner, crest, outer, and patch part of the reef, contains most features greater than this threshold. It also explains the reverse pattern in choice of surface fitting window smaller than 30 m (W2, Fig. 12d). An inappropriate selection of fitting window could overfit the noisy point cloud.

6. Error contributions

In our current workflow, the optimal RMSE in ICESat-2 photon heights is 0.4–0.5 m in Fig. 12d and Table 2. By looking into the numbers in Table 2, STD is about 0.1–0.4 m smaller than RMSE, indicating that the RMSE contains a part of systematic error that may be associated with datum transformation. In other analyses using ICESat-2 validation set (K_{10}) for comparison, datum transformation would not be an issue. Thus, the error budget of ICESat-2 photon heights estimated by our workflow is about 0.2–0.3 m level (STD in Table 2). Regarding to the GoF and RMSE provided in Table 3 and 4, different Sentinel-2 training models yield an error of 0.6–0.9 m for the best 1–2 images (include the error propagated from ICESat-2 photon heights). Even though the error of Sentinel-2 SDB can be further reduced to 0.5–0.8 m by the composite technique developed herein (Fig. 9), there is still a level of error in 0.3–0.5 m to be mitigated. Actually, the error is associated with the number of training samples as indicated by Table 5, Fig. 10, and Fig. 11. An increase of error in 5–13 m deep in Fig. 10, corresponding to the error of Barque Canada and Bombay Reef in Fig. 11, is associated with a poor number of training samples in this range (Table 5, times 9 for the training points). Similarly, a sharp increase of error after 11 m in Dongsha's case is related to the sudden drop of training samples in this range (Table 5). It is obvious that the more and the narrower spread of training samples in Fig. 6, the better constrained curve could be derived. It can also be evident in Scarborough Reef case. Even though the RMSE in Fig. 9 of the composite image is 0.76 m, its performance is among the best in Fig. 11 up to 14 m deep. A sufficient number of training points (Table 5), especially when the scattered points tend to diverge beyond 10 m deep (Fig. 6), is the key to uphold a good performance for a model.

Besides, it is worth noting the contribution of ICESat-2 geolocation error as it is difficult to be cancelled out due to the very limited number of ATL03 transects. The geolocation error could impose first order error in the composite images. We simulate the budget of vertical error that could be attributed to the geolocation error of ICESat-2 footprint (Fig. 14). The calculation follows $\sigma_h = slope \times \sigma_G$, in which σ_h is the photon height error, *slope* is the seafloor slope derived from airborne LiDAR data, and σ_G is the geolocation error in 1–5 m. The simulation is conducted using the geolocation of photons listed in Table 2, and σ_h is computed in the 90th percentile of all photons in each 1-m vertical interval. It is interesting to see that the error distribution is similar to the pattern in Fig. 11 (red circle and blue star). It is because the geolocation-induced error tends to increase when the slope is steeper. The first bulge appears near 4–5 m, a typical location of buttress zone and the reef face. The following increase is in the lagoon (>9 m) where some reef crests appeared within it. The geolocation error around 0.1–0.2 m level in 1–8 m deep could explain a part of error in STD of Table 2. Hence, a more complete study, which remains as our future work, is needed as this issue had been emphasized in many recent studies (Smith et al., 2019; Ma et al., 2020; Neuenschwander et al., 2020). However, the accuracy for over 15 m depth is mainly attributed to environmental conditions and the radiometric limit in Sentinel-2 images.

7. Conclusions

This study overcomes the limitation of traditional methods that need ground truth for the production and verification of SDB, by utilizing a combination of ICESat-2 laser altimetry and Sentinel-2 optical images. We develop an innovative and automatic surface detection algorithm for ICESat-2 ATL03 point clouds to obtain a set of depth measurements with an accuracy of 0.26–0.61 m as compared against airborne LiDAR data. A semi-empirical approach physically based on Stumpf's ratio model (Stumpf et al., 2003) is adopted to develop Sentinel-2 SDB products. We introduce a scheme to produce the composite image that efficiently reduce the error potentially contributed from ICESat-2 ATL03 (both exact vertical accuracy and spatial modeling error), Sentinel-2 radiometric error, and randomly changed diffuse attenuation coefficient in water. The accuracy of the composite SDB for the six islands ranges from 0.50 to 0.90 m by all models. The medians of SDB derived from single images over the six islands could fulfill the requirement of ZOC category *C* within depth < 8 m. However, it is observed that the three empirical models tested in this study have similar performance in all cases. Among them, the Modified Polynomial Ratio model (MPR) slightly outperforms in the final results (Table 4). The improvement from the weighted-average scheme is more significant than the choice of fitting models.

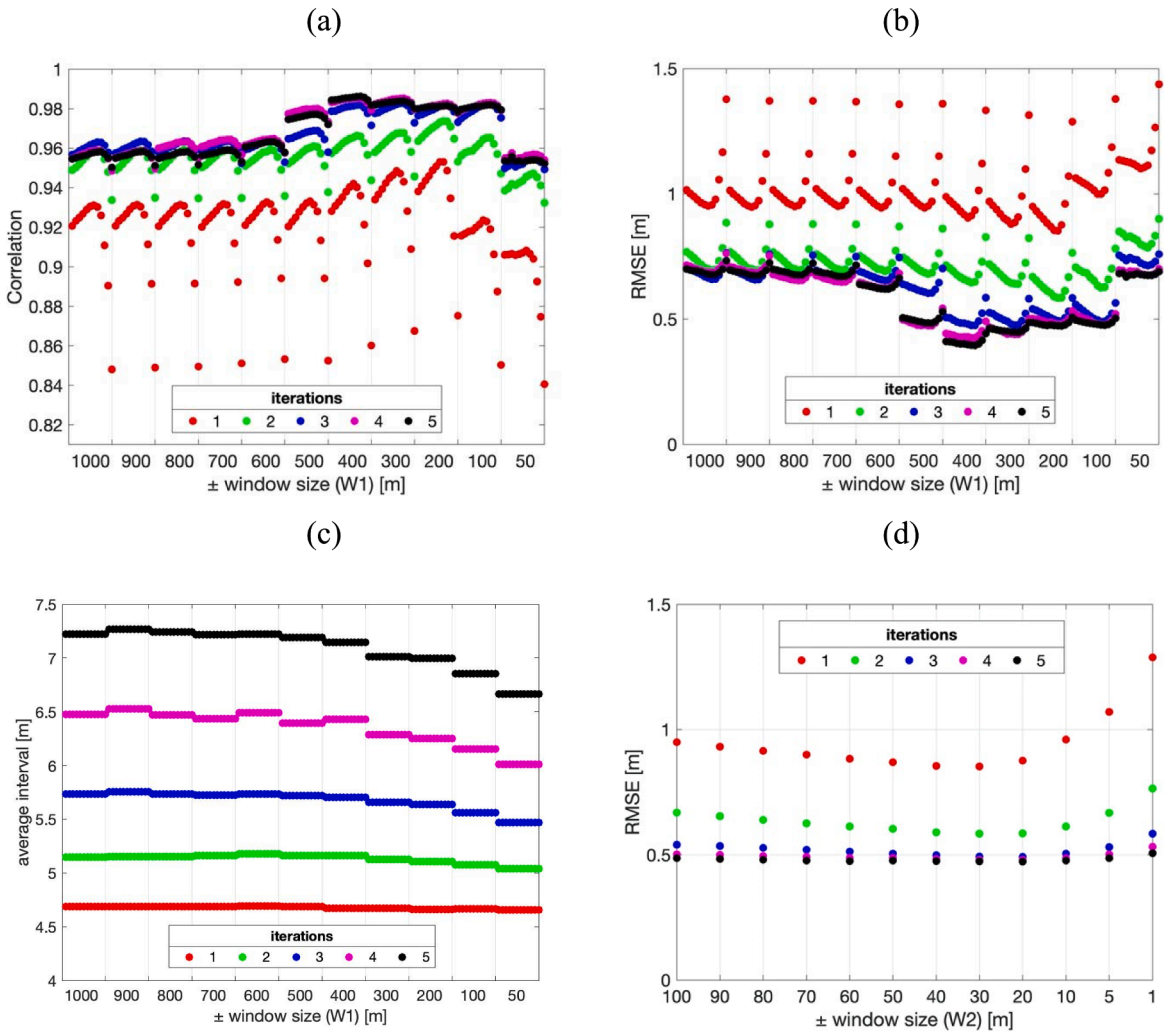

Fig. 12. Variation of accuracy indicators as the change of photon filtering criteria. (a) Correlation changes with different W1, W2, and iterations. (b) RMSE changes with the same scenarios. (c) Average interval changes with the same scenarios. (d) Zoom-in view of panel (b) in W1 = 200.

Table 6
Variables used to examine the error budget in ICESat-2 photon height estimate.

Variables	Options
Window size for point cloud filtering (W1) [m]	1000, 900, 800, 700, 600, 500, 400, 300, 200, 100, 50
Iteration [times]	1, 2, 3, 4, 5
Window size for surface fitting (W2) [m]	100, 90, 80, 70, 60, 50, 40, 30, 20, 10, 5, 1

This paper's main contribution is to introduce a workflow to integrate ICESat-2 and Sentinel-2 for bathymetry retrieval in islands that are poorly mapped or difficult to access. However, it is still known that ICESat-2 may have limited overpasses near small islands. The presence of clouds leads to very limited photons hitting the ground. In addition, Sentinel-2 also experiences surface condition issues, such as weather forcing (e.g., fog, rain, humid atmosphere) and clouds/shadows. SDB may have deteriorated qualities in those images or under unfavored water clarity (suspended solids, algae, pollution, etc.), even in very shallow waters with a few meters deep. Ground survey is suggested to ensure the reliability of nautical charts in these areas.

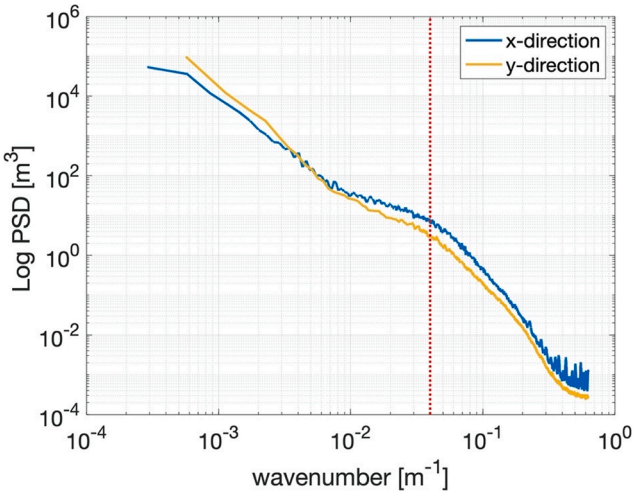

Fig. 13. Power spectral density of the seafloor derived from airborne LiDAR data.

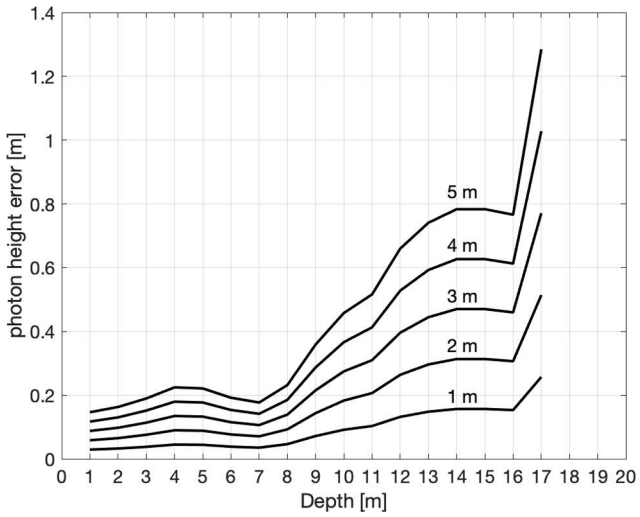

Fig. 14. Simulation of vertical error of photon height as induced by 1–5 m geolocation error in 10 ground tracks in Table 2.

Declaration of Competing Interest

The authors declare that they have no known competing financial interests or personal relationships that could have appeared to influence the work reported in this paper.

Acknowledgement

This work was supported in part by the Ministry of Science and Technology (MOST), Taiwan under project number 107-2119-M-008-021, 108- 2621-M-008-001, and in part, by the Ministry of the Interior project number 109CCL042C.

References

Adler-Golden, S.M., Acharya, P.K., Berk, A., Matthew, M.W., Gorodetzky, D., 2005. Remote bathymetry of the littoral zone from AVIRIS, LASH, and QuickBird imagery. IEEE Transactions on Geoscience and Remote Sensing 43 (2), 337–347.

Albright, A., Glennie, C., 2020. Nearshore Bathymetry From Fusion of Sentinel-2 and ICESat-2 Observations. IEEE Geoscience and Remote Sensing Letters.

Andersen, O., Knudsen, P., Stenseng, L., 2018. A New DTU18 MSS Mean Sea Surface-Improvement from SAR Altimetry. In 25 years of progress in radar altimetry symposium.

Caballero, I., Stumpf, R.P., 2020. Towards routine mapping of shallow bathymetry in environments with variable turbidity: contribution of Sentinel-2A/B satellites mission. Remote Sensing 12 (3), 451.

Cahalane, C., Magee, A., Monteys, X., Casal, G., Hanafin, J., Harris, P., 2019. A comparison of Landsat 8, RapidEye and Pleiades products for improving empirical predictions of satellite-derived bathymetry. Remote Sensing of Environment 233, 111414.

Chénier, R., Faucher, M.A., Ahola, R., 2018. Satellite-derived bathymetry for improving Canadian Hydrographic Service charts. ISPRS International Journal of Geo-Information 7 (8), 306.

Dahlgren, T.G., Schläppy, M.L., Šaškov, A., Andersson, M.H., Rzhanov, Y., Fer, I., 2014. Assessing the impact of windfarms in subtidal, exposed marine areas. In: Marine Renewable Energy Technology and Environmental Interactions. Springer, Dordrecht, pp. 39–48.

Drusch, M., Del Bello, U., Carlier, S., Colin, O., Fernandez, V., Gascon, F., Meygret, A., 2012. Sentinel-2: ESA's optical high-resolution mission for GMES operational services. Remote sensing of Environment 120, 25–36.

Eugenio, F., Marcello, J., Martin, J., 2015. High-resolution maps of bathymetry and benthic habitats in shallow-water environments using multispectral remote sensing imagery. IEEE Transactions on Geoscience and Remote Sensing 53 (7), 3539–3549.

Forfinski-Sarkozi, N.A., Parrish, C.E., 2016. Analysis of MABEL bathymetry in Keweenaw bay and implications for ICESat-2 ATLAS. Remote Sensing 8 (9), 772.

Gao, B.C., Montes, M.J., Davis, C.O., Goetz, A.F., 2009. Atmospheric correction algorithms for hyperspectral remote sensing data of land and ocean. Remote sensing of environment 113, S17–S24.

Gascon, F., Bouzinac, C., Thépaut, O., Jung, M., Francesconi, B., Louis, J., Languille, F., 2017. Copernicus Sentinel-2A calibration and products validation status. Remote Sensing 9 (6), 584.

Geyman, E.C., Maloof, A.C., 2019. A simple method for extracting water depth from multispectral satellite imagery in regions of variable bottom type. Earth and Space Science 6 (3), 527–537.

Green, E., Mumby, P., Edwards, A., Clark, C., 2000. Remote Sensing: Handbook for Tropical Coastal Management. United Nations Educational, Scientific and Cultural Organization (UNESCO).

Hodúl, M., Bird, S., Knudby, A., Chénier, R., 2018. Satellite derived photogrammetric bathymetry. ISPRS Journal of Photogrammetry and Remote Sensing 142, 268–277.

Yuan, C., Gong, P., Bai, Y., 2020. Performance assessment of ICESat-2 laser altimeter data for water-level measurement over lakes and reservoirs in China. Remote Sensing 12 (5), 770.

IHO, S. 67,(2017). Mariners' Guide to Accuracy of Electronic Navigational Charts (ENC). Edition 0.4, International Hydrographic Organization, Monaco, April.

Jasinski, M., Stoll, J., Cook, W., Ondrusek, M., Stengel, E., 2016. Inland and Near Shore Water Profiles Derived from the High Altitude, Multiple Altimeter Beam Experimental Lidar (MABEL). Journal of Coastal Research 76 (sp1), 44–55.

Kalnay, E., Kanamitsu, M., Kistler, R., Collins, W., Deaven, D., Gandin, L., Iredell, M., Saha, S., White, G., Woollen, J., Zhu, Y., Chelliah, M., Ebisuzaki, W., Higgins, W., Janowiak, J., Mo, K.C., Ropelewski, C., Wang, J., Leetmaa, A., Reynolds, R., Jenne, R., Joseph, D., 1996. The NCEP/NCAR 40-year reanalysis project. Bulletin of the American meteorological Society 77 (3), 437–472.

Kerr, J.M., Purkis, S., 2018. An algorithm for optically-deriving water depth from multispectral imagery in coral reef landscapes in the absence of ground-truth data. Remote sensing of environment 210, 307–324.

Knudby, A., Ahmad, S.K., Ilori, C., 2016. The potential for Landsat-based bathymetry in Canada. Canadian Journal of Remote Sensing 42 (4), 367–378.

Lee, Z., Carder, K.L., Mobley, C.D., Steward, R.G., Patch, J.S., 1998. Hyperspectral remote sensing for shallow waters. I. A semianalytical model. Applied optics 37 (27), 6329–6338.

Lee, Z., Carder, K.L., Mobley, C.D., Steward, R.G., Patch, J.S., 1999. Hyperspectral remote sensing for shallow waters: 2. Deriving bottom depths and water properties by optimization. Applied optics 38 (18), 3831–3843.

Lee, Z., Weidemann, A., Arnone, R., 2012. Combined Effect of reduced band number and increased bandwidth on shallow water remote sensing: The case of worldview 2. IEEE Transactions on Geoscience and Remote Sensing 51 (5), 2577–2586.

Li, Y., Gao, H., Jasinski, M.F., Zhang, S., Stoll, J.D., 2019. Deriving High-Resolution Reservoir Bathymetry from ICESat-2 Prototype Photon-Counting Lidar and Landsat Imagery. IEEE Transactions on Geoscience and Remote Sensing 57 (10), 7883–7893.

López-Serrano, P.M., Corral-Rivas, J.J., Díaz-Varela, R.A., Álvarez-González, J.G., López-Sánchez, C.A., 2016. Evaluation of radiometric and atmospheric correction algorithms for aboveground forest biomass estimation using Landsat 5 TM data. Remote sensing 8 (5), 369.

Louis, J., Debaecker, V., Pflug, B., Main-Knorn, M., Bieniarz, J., Mueller-Wilm, U., ... & Gascon, F. (2016, May). Sentinel-2 sen2cor: L2a processor for users. In Proceedings of the Living Planet Symposium, Prague, Czech Republic (pp. 9-13).

Lyzenga, D.R., 1978. Passive remote sensing techniques for mapping water depth and bottom features. Applied optics 17 (3), 379–383.

Lyzenga, D.R., 1981. Remote sensing of bottom reflectance and water attenuation parameters in shallow water using aircraft and Landsat data. International journal of remote sensing 2 (1), 71–82.

Ma, Y., Xu, N., Liu, Z., Yang, B., Yang, F., Wang, X.H., Li, S., 2020. Satellite-derived bathymetry using the ICESat-2 lidar and Sentinel-2 imagery datasets. Remote Sensing of Environment 250, 112047.

Markus, T., Neumann, T., Martino, A., Abdalati, W., Brunt, K., Csatho, B., Farrell, S., Fricker, H., Gardner, A., Harding, D., Jasinski, M., Kwok, R., Magruder, L., D. Lubin, D., Luthcke, S., Morison, J., Nelson, R., Neuenschwander, A., Palm, S., Popescu, S., Shum, C., Schutz, B. E., Smith, B., Yang, Y., and Zwally, J. (2017). "The Ice, Cloud, and land Elevation Satellite-2 (ICESat-2): Science requirements, concept, and implementation." Remote Sensing of Environment, 190, 260-273.

Martino, A. J., Neumann, T. A., Kurtz, N. T., & McLennan, D. (2019). ICESat-2 mission overview and early performance. In Sensors, Systems, and Next-Generation Satellites XXIII (Vol. 11151, p. 111510C). International Society for Optics and Photonics.

Masselink, G., Beetham, E., Kench, P., 2020. Coral reef islands can accrete vertically in response to sea level rise. Science. Advances 6 (24), eaay3656.

McCombs, M.P., Mulligan, R.P., Boegman, L., 2014. Offshore wind farm impacts on surface waves and circulation in Eastern Lake Ontario. Coastal Engineering 93, 32–39.

Mobley, C.D., 1995. The optical properties of water. Handbook of Optics.

Nazeer, M., Nichol, J.E., Yung, Y.K., 2014. Evaluation of atmospheric correction models and Landsat surface reflectance product in an urban coastal environment. International journal of remote sensing 35 (16), 6271–6291.

Neuenschwander, A., Popescu, S., Nelson, R., Harding, D., Pitts, K., Robbins, J., Sheridan, R., 2019. Ice, Cloud, and Land Elevation 1 Satellite 2 (ICESat-2) Algorithm Theoretical Basis Document (ATBD) for Land-Vegetation Along-Track Products (ATL08) release 002. National Aeronautics and Space Administration, Goddard Space Flight Centre.

Neuenschwander, A., Guenther, E., White, J.C., Duncanson, L., Montesano, P., 2020. Validation of ICESat-2 terrain and canopy heights in boreal forests. Remote Sensing of Environment 251, 112110.

Neumann, T. A., A. Brenner, D. Hancock, J. Robbins, S. B. Luthcke, K. Harbeck, J. Lee, A. Gibbons, J. Saba, and K. Brunt. (2019a). ATLAS/ICESat-2 L2A Global Geolocated Photon Data, Version 1. Boulder, Colorado USA. NSIDC: National Snow and Ice Data Center. doi: https://doi.org/10.5067/ATLAS/ATL03.001. [Date Accessed].

Neumann, T.A., Martino, A.J., Markus, T., Bae, S., Bock, M.R., Brenner, A.C., Harbeck, K., 2019b. The Ice, Cloud, and Land Elevation Satellite–2 Mission: A global

geolocated photon product derived from the advanced topographic laser altimeter system. Remote sensing of environment 233, 111325.
Neumann, T., Brenner, A., Hancock, D., Robbins, J., Saba, J., Harbeck, K., & Gibbons, A. (2019). Ice, Cloud, and land Elevation Satellite–2 (ICESat-2) Project: Algorithm Theoretical Basis Document (ATBD) for Global Geolocated Photons (ATL03). National Aeronautics and Space Administration, Goddard Space Flight Center.
Neumann, T. A., A. Brenner, D. Hancock, J. Robbins, J. Saba, K. Harbeck, A. Gibbons, J. Lee, S. B. Luthcke, T. Rebold, et al. 2020. ATLAS/ICESat-2 L2A Global Geolocated Photon Data, Version 3. Boulder, Colorado USA. NASA National Snow and Ice Data Center Distributed Active Archive Center. doi: https://doi.org/10.5067/ATLAS/ATL03.003. [Date Accessed].
Pacheco, A., Horta, J., Loureiro, C., Ferreira, Ó., 2015. Retrieval of nearshore bathymetry from Landsat 8 images: A tool for coastal monitoring in shallow waters. Remote Sensing of Environment 159, 102–116.
Parrish, C.E., Magruder, L.A., Neuenschwander, A.L., Forfinski-Sarkozi, N., Alonzo, M., Jasinski, M., 2019. Validation of ICESat-2 ATLAS Bathymetry and Analysis of ATLAS's Bathymetric Mapping Performance. Remote Sensing 11 (14), 1634.
Pike, S., Traganos, D., Poursanidis, D., Williams, J., Medcalf, K., Reinartz, P., Chrysoulakis, N., 2019. Leveraging Commercial High-Resolution Multispectral Satellite and Multibeam Sonar Data to Estimate Bathymetry: The Case Study of the Caribbean Sea. Remote Sensing 11 (15), 1830.
Poursanidis, D., Traganos, D., Chrysoulakis, N., Reinartz, P., 2019. Cubesats Allow High Spatiotemporal Estimates of Satellite-Derived Bathymetry. Remote Sensing 11 (11), 1299.
Sandwell, D.T., Müller, R.D., Smith, W.H., Garcia, E., Francis, R., 2014. New global marine gravity model from CryoSat-2 and Jason-1 reveals buried tectonic structure. Science 346 (6205), 65–67.
Sagawa, T., Yamashita, Y., Okumura, T., Yamanokuchi, T., 2019. Satellite Derived Bathymetry Using Machine Learning and Multi-Temporal Satellite Images. Remote Sensing 11 (10), 1155.
Smith, B., Fricker, H.A., Holschuh, N., Gardner, A.S., Adusumilli, S., Brunt, K.M., Nilsson, J., 2019. Land ice height-retrieval algorithm for NASA's ICESat-2 photon-counting laser altimeter. Remote Sensing of Environment 233, 111352.
Shih, P.T.Y., Arumugam, D., Shyue, S.W., 2011. Bathymetric Lidar Survey Of Penghu Islands and Dongsha Atoll Using an Ellipsoidal Height System for Bathymetric Mapping In Shallow Waters and Difficult-to-Navigate Environments. Sea Technology 52 (11), 42–45.
Stumpf, R.P., Holderied, K., Sinclair, M., 2003. Determination of water depth with high-resolution satellite imagery over variable bottom types. Limnology and Oceanography 48 (1part2), 547–556.
Sturges, H.A., 1926. The choice of a class interval. Journal of the American Statistical Association 21 (153), 65–66.
Traganos, D., Poursanidis, D., Aggarwal, B., Chrysoulakis, N., Reinartz, P., 2018. Estimating satellite-derived bathymetry (SDB) with the google earth engine and sentinel-2. Remote Sensing 10 (6), 859.
Vermote, E.F., Tanré, D., Deuze, J.L., Herman, M., Morcette, J.J., 1997. Second simulation of the satellite signal in the solar spectrum, 6S: An overview. IEEE transactions on geoscience and remote sensing 35 (3), 675–686.
Weintrit, A., 2018. Accuracy of bathymetric data in electronic navigational charts. Zeszyty Naukowe Akademii Morskiej w Szczecinie.
Wilson, R.T., 2013. Py6S: A Python interface to the 6S radiative transfer model. Computers & Geosciences 51 (2), 166.